Fermi National Accelerator Laboratory
Summer School 2023

Thermal Analysis of the Bus Bars for the 800MeV Injection Era

Silvia Picchi
Università di Pisa

Victor Grzelak
Supervisor

Contents

The work presented in this report has been carried during a 9-weeks internship at IARC, Fermilab. Over the course of these weeks I have been working under the guidance of Victor Grzelak, Engineer Physicist at Fermilab, to complete the thermal analysis of some components of the synchrotron Booster, a proton accelerator that is planned to be improved with the PIP-II (Proton Improvement Plan II) project.

This experience has been fundamental in my growth as an engineer and I am truly grateful for the opportunity to meet and work with such amazing people.

Figure 1: Moments.

1 Introduction

Fermilab is the premier particle physics and accelerator laboratory of the United States. It is located in Batavia, Illinois and is managed by the Fermi Research Alliance LLC for the U.S. Department of Energy Office of Science.

Since 1967, physicist and engineers from all around the world work to answer to enhance the understanding of everything we see around us. The mission of Fermilab is to solve the mysteries of matter, energy, space and time for the benefit of all.

IARC (Illinois Accelerator Research Center) is a part of the Fermi National Accelerator Laboratory and its aim is to advance the development of technology in cooperation with industrial partners. It consists of a huge area which provides space and infrastructures for the scientists from Fermilab, Argonne National Laboratory, local universities and industries to turn new ideas in accelerator technology into viable commercial products.

In addition to office and classroom space, IARC provides areas for test accelerators, cryogenics infrastructure, temperature-controlled work spaces, high-capacity electrical power systems and industrial cooling water.

1.1 Proton Improvement Plan-II

Among the many project carried at IARC there is the **Proton Improvement Plan II (PIP-II)**, an enhancement to the Fermilab accelerator complex. PIP-II will deliver high-power proton beams to enable muon or neutrino based experiments, such as DUNE. PIP-II addresses two of the

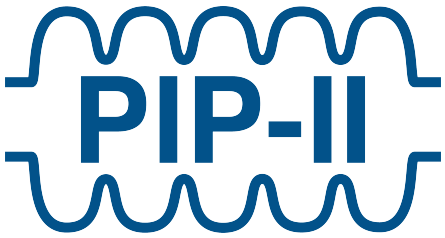

Figure 2: PIP-II Logo. © Fermilab

missions of the High Energy Physics program:

> "To illuminate and answer questions about the unification of the forces of nature, the nature and origin of dark energy and dark matter, and the origins of the universe,
>
> to deliver scientific breakthroughs and extend our knowledge of the natural world by capitalizing on the capabilities available at the national laboratories, and through partnerships with universities and industry."

This project consists in **building a brand-new radio-frequency linear accelerator** that will be able to inject higher energy proton beams in the Booster (the proton synchrotron), and in **improving the Booster** itself. Upon completion, the new linar accelerator will accelerate protons at up to 800 MeV, over its 215-meter length, with an instantaneous beam power of more than 1 megawatt. The increase in the beam energy brings many technical challenges, some of which will be addressed in this report.

The present linar accelerator, the **Linac**, accelerates proton beams up to 400MeV. The beam that is extracted from the Linac enters the Booster synchrotron and is then accelerated to a kinetic energy of 8GeV. Booster is a rapid cycling synchrotron (RCS), with a present machine frequency of 15 Hz.

The beam extracted from the Booster is injected into the **Recycler**, which is a non-accelerating synchrotron, and then it is finally injected in the **Main Injector**, which is the final accelerating synchrotron at Fermilab. Here the beam is accelerated from 8GeV to 120GeV and about $5.6 \cdot 10^{13}$ protons are extracted from the MI and collide with a target, generating pions that decay into neutrinos for Fermilab's neutrino experiments.

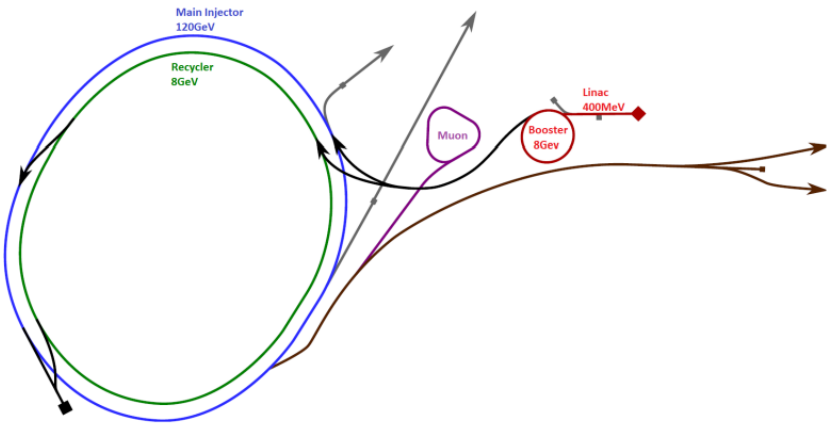

Figure 3: Present day Fermilab accelerator complex layout

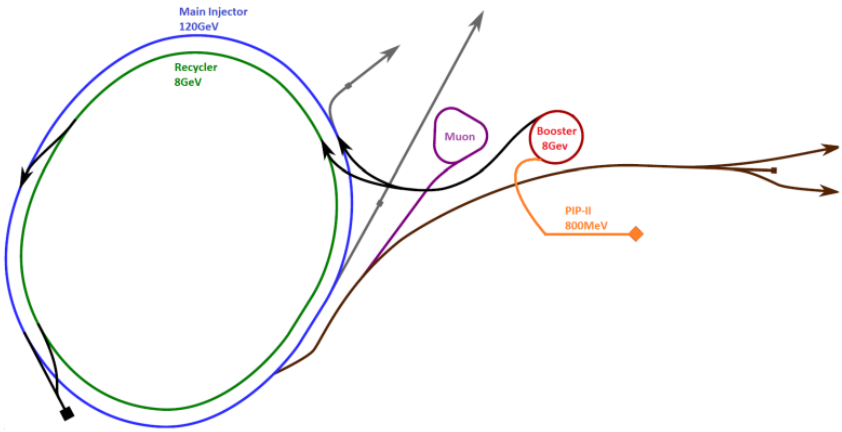

Figure 4: Fermilab accelerator complex layout in PIP-II era with new Linac

As previously stated, the PIP-II upgrade seeks to **double the injection energy** and is designed to inject $6.5 \cdot 10^{12}$ protons into the Booster at 800MeV. The project also plans to **increase the Booster machine frequency** from 15 Hz to 20 Hz. This change will result in a steeper momentum time profile, and more RF voltage will be required.

	Original	Present	PIP-II	
Linac Extraction Kinetic Energy	200	400	800	MeV
Booster Injection Frequency f_{RF}	30.1	37.9	44.7	MHz
Booster Extraction Frequency f_{RF}	52.808	52.808	52.808	MHz
Booster Extraction Kinetic Energy	8	8	8	GeV
Booster Cycle Time	66.6	66.6	50	ms

Table 1: Comparison of machine parameters

The core question that needs to be answered is: can the current infrastructure and cavities handle the change in operating conditions?

To give an answer to this question, many infrastructures and components need to be tested and eventually redesigned. This report will focus on the **thermal problem** expected in the new working conditions of the **bus bars**.

For further information: [3] [1]

1.2 Purpose of the internship

My intership at IARC has been focused on the thermal analysis of the bus bars of the Booster. The bus bars are the conductors that bring the bias current from the bias supply to the ferrite tuners in each RF cavity of the synchrotron. Since they are not superconductors, during normal operations they will heat up due to the Joule effect.
The goal of my work is to build a model of the bus bars assembly that describes effectively the experimental data and that can be used to predict the temperature increase and distribution among the components of the assembly, in present and future operational conditions.

The Booster synchrotron
The Booster is a circular proton accelerator with a circumference of 474.2m and **22 RF cavities**. Each cavity and its dedicated systems will be referred to as a **station**, while the location between the galleries and the tunnel is called the **penetration**. The ring has been in operation since the early 1970's and originally had 16 RF stations, increased to 22 over the course of the years.

A general scheme of the system can be seen in figure 5, while figure **??** shows the penetration opening section, where the bus bars are placed.

These figures refer to cavities 19 and 20. Not all cavities share exactly the same geometry, but this is a good representation of the system.

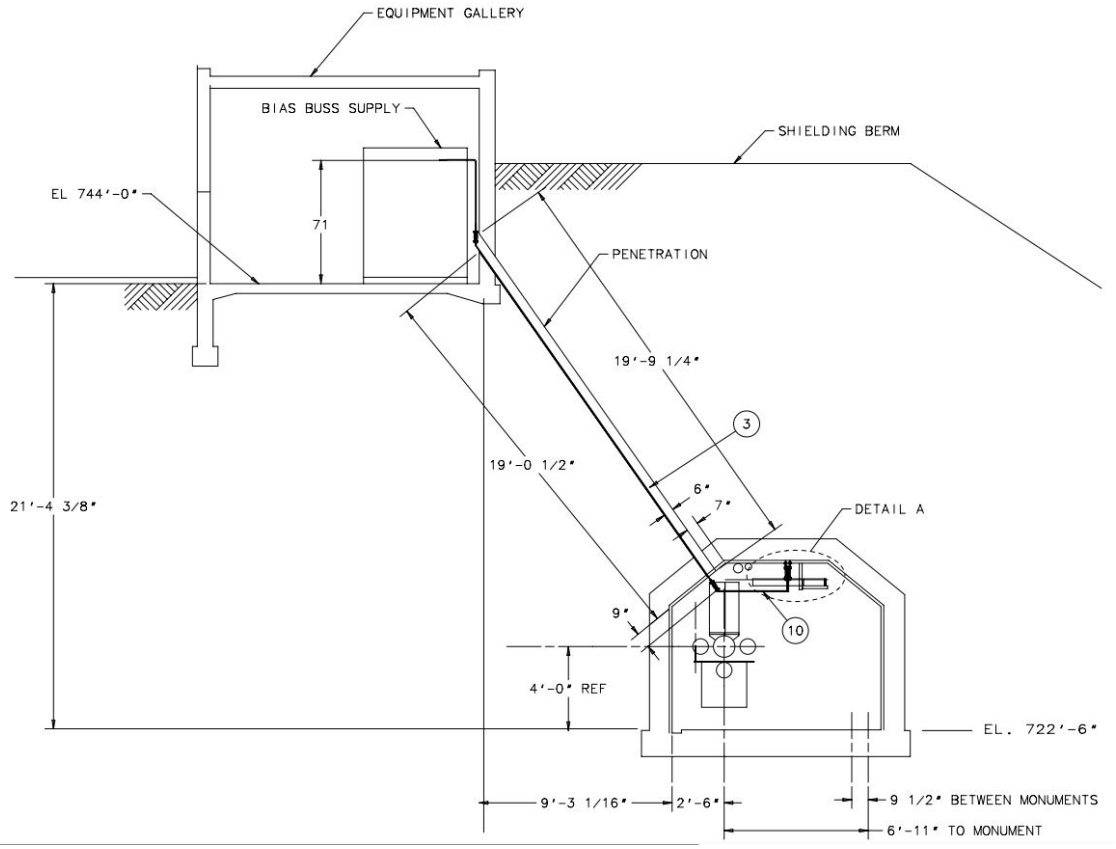

Figure 5: Booster RF cavity upgrade stations 19 and 20, penetration to cavity layout. © Fermilab

③ cavity bus bar assembly
⑩ penetration to bus bars

Among the components of each station there are the **bus bars**, conductors used for electrical power distribution. The bus bars bring bias current (see figure 7) from the bias supply to the ferrite tuners in order to change the resonance frequency of the accelerating cavities. In simple words, the bias current basically allow to vary the magnetic permeability of the ferrites and therefore the inductance of the cavities, which can be thought of as LC circuits, so changing the L allows to change the resonance frequency.

The busbars are individually wrapped in Kapton tape, a type of polyimide tape developed by DuPont in the 1960s, used for electrical and thermal insulation- the two bars have a dielectric sheet sandwiched between them, for further electrical insulation, made of Nomex paper. The assembly is then wrapped in a second layer of Kapton tape and then protected an aluminum clampshell, which made of 2 c-sections.

Figure 6 shows a scheme of the described assembly, while figures 8, 9, 10 and 11 show some actual pictures for the bus bars assembly, as seen from the booster gallery and from the tunnel.

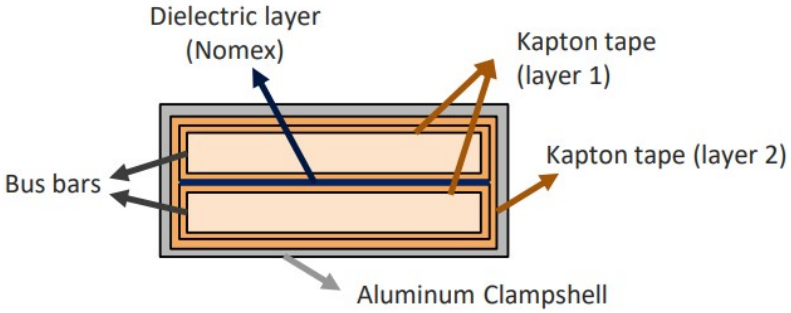

Figure 6: Bus bars assembly section

The power supplies are situated in the galleries and the location between the galleries and the tunnel is referred to as the **penetration**. The penetration is filled with several feet of **polyethylene beads** used for radiation shielding, which have a melting temperature of about 120°C.

Some preliminary test with the PIP-II working conditions showed clearly that the polyethylene beads would reach their melting temperature. At 20Hz, the temperature reached 100°C within the first 6 hours operating and was still significantly increasing- forecasting the trend, the test was stopped.

Figure 7 shows the current curve as a function of time for 15Hz and 20Hz working conditions. The horizontal lines highlighted in the figure are the RMS current values for the two curves.

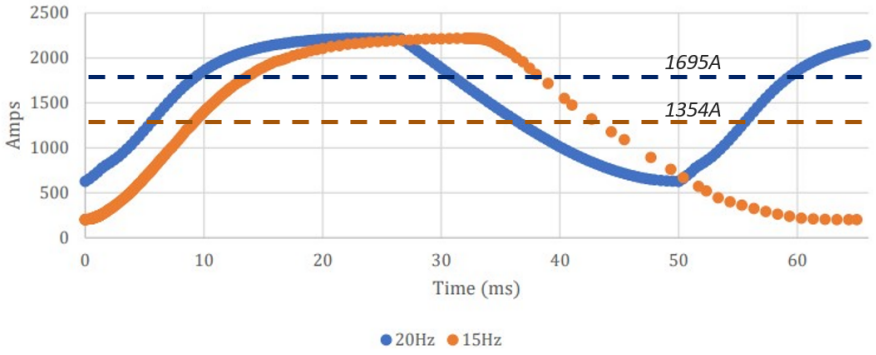

Figure 7: Bias current curve

Figure 8: Bus bars behind the bias supply

Figure 9: Bus bars as seen from the gallery (Booster station 10)

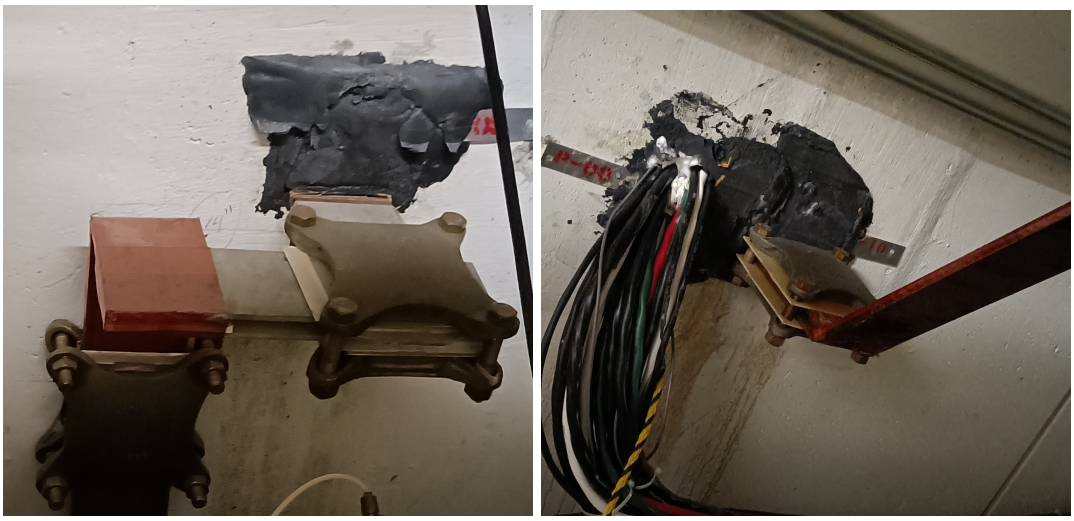

Figure 10: Bus bars as seen from the tunnel

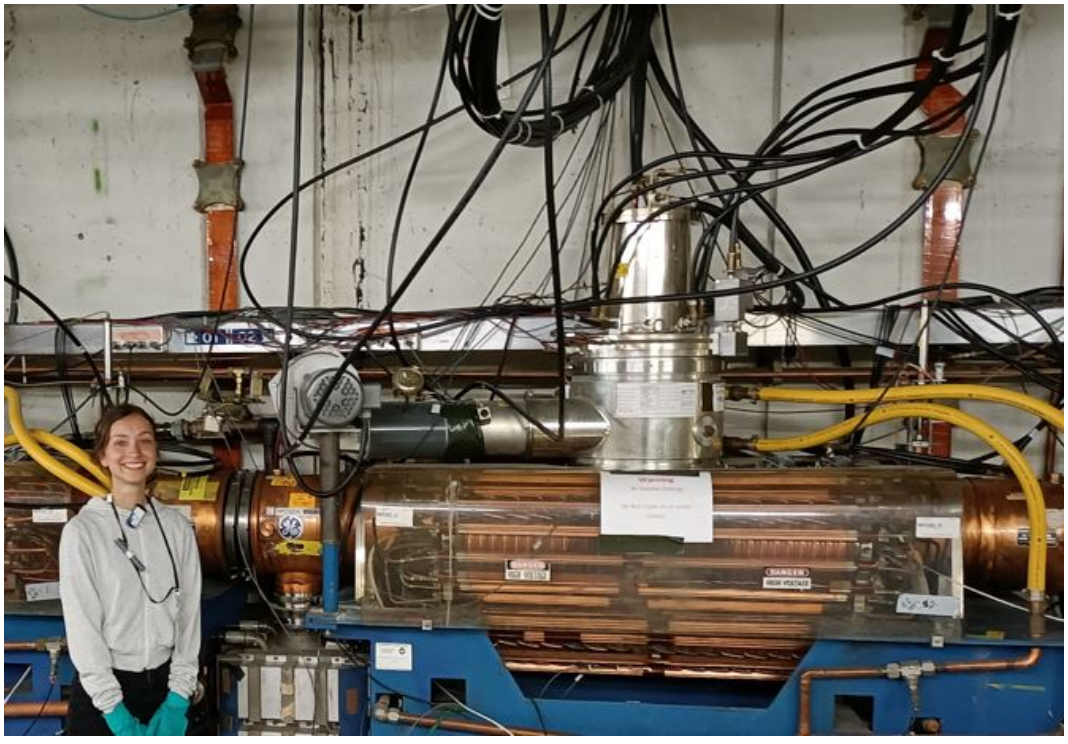

Figure 11: View of the bus bars and RF cavities in the Booster tunnel.

2 Thermal analysis

In this section the thermal analysis of the bus bars will be presented. This work has been carried starting from the simplest kind of analysis, and from there adding layers of complexity to the model.

Variables

U	Internal energy	J
Q	Heat flux	J
$\dot{Q}$	Thermal power	W
ρ	density	kg/m^3
V	volume	m^3
c_p	heat capacity	J/kgK
A	area	m^2
L	length	m
b	cross section width	m
h	cross section height	m
T	temperature	K
T_∞	environment temperature	K
k	conduction coefficient	$W/(m^2K)$
$\bar{h}$	convection coefficient	$W/(mK)$
ϵ	emissivity	[-]
σ	Boltzmann's constant	$W/(m^2K^4)$
R	electric resistance	Ω
Bi	Biot number	[-]
f	frequency	MHz
I_{RMS}	current root mean square	A

2.1 Lumped parameters analysis

A lumped parameter model is a zero-dimensional representation of a generic physical system, assuming all the components of the system can be described as points or 'lumps'. In the case when the body has an almost uniform internal temperature and so the internal temperature gradients are small, it is possible to 'lump' all the heat capacitance at a single body temperature, $T(\vec{x}, t) = T(t)$.

It is possible to write a simple energy balance on the body according to the First Law:

$$\dot{Q} = \frac{dU}{dt} \tag{1}$$

$$\dot{Q} = \frac{d}{dt}[\rho c V (T - T_{ref})] \tag{2}$$

In the case in analysis, the balance will include convection, irradiation and the power generation due to the Joule effect $\dot{Q}_{joule} = I^2 R$:

$$-\bar{h}A(T - T_\infty) - \varepsilon\sigma A(T^4 - T_\infty^4) + \dot{Q}_{joule} = \rho c V \frac{d(T - T_{ref})}{dt} \tag{3}$$

It is worth noticing that thermal conductivity is missing from this equation- this is a consequence of the assumption that the temperature of the body is nearly uniform, and internal conduction is not important. In order to validate this assumption, there is an adimensional parameter that must be evaluated:

$$Bi = \frac{\bar{h}L}{k} \tag{4}$$

The group $\bar{h}L/k$ is called the ***Biot number***. In the case $Bi << 1$ it can be assumed that the temperature variation within the body is negligible. The **lumped capacity solution** will normally be accurate within about 3% if $Bi < 0.1$, and more accurate as Bi gets smaller (ref. [4]).

Lumped capacity analysis can be used for both steady-state solutions and transient solutions.

2.1.1 Preliminary calculations for a single bus bar

The first step of the work will be the analysis of a single bus bar in open air. The purpose of this very simple calculations will be to validate the lumped capacity analysis described in the previous section, in order to use it for further calculation with more accurate boundary conditions.
To do so, the calculations will be compared with experimental data available in the **ampacity tables**. These tables allow to predict the **temperature rise** for a copper bus bar with a specific cross section which is carrying a specific amount of current.

Table 2 summarizes the data used for the calculation:

Cross section width b	4"	Resistance R	8.32 $\mu\Omega$·ft.
Cross section height h	$\frac{1}{4}''$	Emissivity ε	0.4
Length L	20'	Convection coefficient $\bar{h}$	3 W/m^2K
Heat conductivity k	398 W/mK	Environment temperature T_∞	40°C

Table 2: 4x1/4" bus bars data and environment data

The environmental data comes from the ampacity tables.
The first step is to calculate Biot number to make sure lumped capacity is going to be an accurate approximation:

$$Bi = \frac{\bar{h}L}{k} = 0.0459 \tag{5}$$

And the second step is to solve equation 3, which is a nonlinear equation, so it will be solved iteratively for three different current levels.

I	T_{steady}	ΔT_{rise}	error
1250 A	71.37°C	31.37°C	4.6%
1700 A	94.76°C	54.76°C	9.5%
1950 A	109.4°C	69.41°C	6.8%

Table 3: Steady-state temperatures for different current levels

These results can be compared to those presented on the ampacity table for this particular bus bars (section, material, working conditions. ref. [5]) to check if the datasets match. The error between calculations and table data can be viewed in table 3. The graph in figure 12 shows the comparison of the rise in temperature from ambient temperature to steady-state conditions- there is a 3-5°C offset from the two sets of values.

The same calculations can be made for the 5x3/8" section bus bars, after checking if the condition $Bi << 1$ is satisfied. The results are summarised in the table 4 and figure 13.

$$Bi = \frac{\bar{h}L}{k} = 0.0459 \tag{6}$$

I	T_{steady}	ΔT_{rise}	error
1800 A	67.63°C	27.63°C	−7.9%
2400 A	86.85°C	46.85°C	−6.3%
2800 A	101.5°C	61.46°C	−5.45%

Table 4: Steady-state temperatures for different current levels

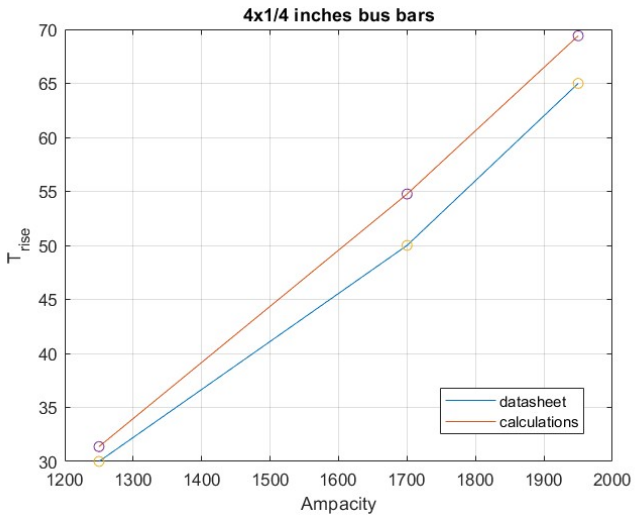

Figure 12: Comparison of calculations and ampacities data

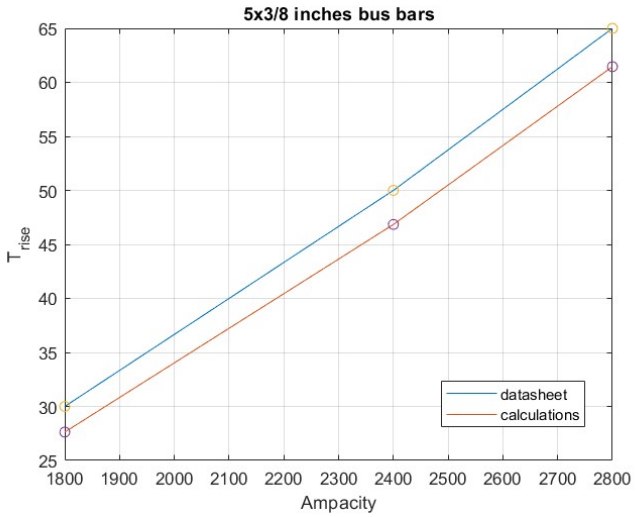

Figure 13: Comparison of calculations and ampacities data

2.1.2 Preliminary calculations for two bus bars

Since the previous calculations agree to a reasonable extent with the expected values, the model described by equation 3 can be used with an added level of complexity- taking into consideration that there are going to be **two bus bars** (one to bring the current from the supply to the cavity, the other to return the current to the supply).

Given the same dimensions and environmental conditions, it is possible to interfere that the calculated values will not agree with the ampacity tables, since the model now has a double resistance (2 bus bars $\rightarrow 2R$) and a lateral area (the surface that can dissipate heat to the environment) that is only slightly larger than the previous case.

As shown in figure 14, this case deviates from the results described in the tables. As previously stated, the increase in the ΔT_{rise} was expected to be slighlty less than double the tables' values, and that is what the calculations show.

It is possible then to change some of the parameters of this two bus bars model, from the ones described in the ampacity tables to more accurate operational conditions:

$$\begin{aligned} T_\infty = 40°\text{C} \quad &\rightarrow \quad T_\infty = 25°\text{C} \\ \varepsilon = 0.4 \quad &\rightarrow \quad \varepsilon = 0.95 \end{aligned}$$

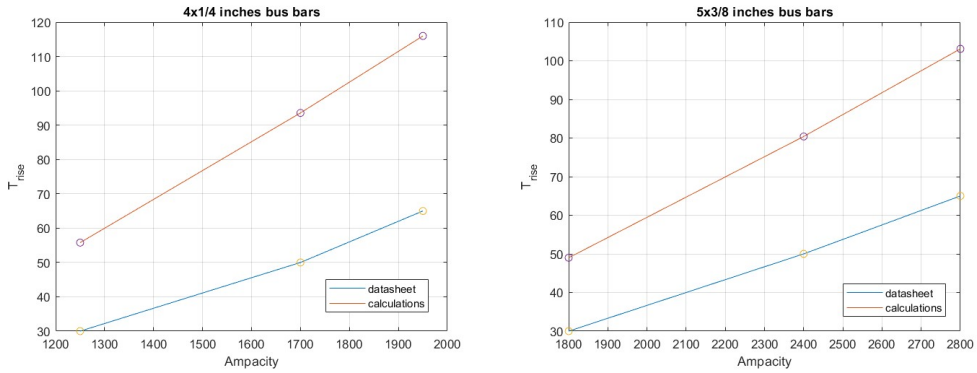

Figure 14: Comparisons for 2 bus bars

Ambient temperature is set at the typical value of 25°C, while the emissivity is considerably higher because the copper of the bus bars will be wrapped in a thin foil of Kapton tape, a material that has a very high emissivity. All the other parameters stay the same.

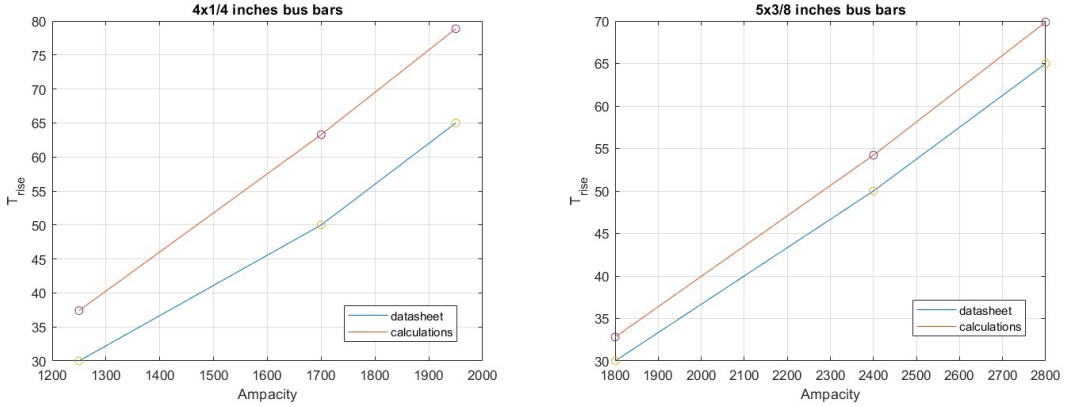

Figure 15: Comparison for 2 bus bars, working conditions

Increasing the radiative heat loss results inevitably in lowering the temperature rise of the bars.

2.1.3 Calculations in actual working conditions

In this section, the same lumped-capacity model described by equation 3 will be used to calculate the steady-state temperature of the two different bus bar in actual operative conditions- which include, finally, the effective RMS current.

There are three cases to be investigated:

- Present conditions (15Hz machine cycle, 400MeV extraction kinetic energy), 4x1/4" bus bars, 1354 ARMS.
  These calculations can be compared with actual measurements of the bus bars working in the Booster;
- PIP-II conditions (20Hz machine cycle, 800MeV extraction kinetic energy), 4x1/4" bus bars, 1695 ARMS.
  Tests suggest that the bus bars temperature will reach over 120°C, that is the melting point of the poly-beads;
- PIP-II conditions (20Hz machine cycle, 800MeV extraction kinetic energy), 5x3/8" bus bars, 1695 ARMS.
  Increasing the cross section of the bus bars will result in decreasing the resistance (thus the heat generation) and having more mass (and thus heat capacity)- for these reasons, this configuration is expected to be able to work at lower temperature and keeping all the components in safe conditions.

Present conditions, 4x1/4"
Table 5 summaries the conditions of the first analysis, while figure 16 shows the evolution of the temperature of the bus bars $T(t)$.

Cross section width b	4"	Resistance R	161.79 $\mu\Omega$
Cross section height h	$\frac{1}{4}$"	Emissivity ε	0.95
Length L	20'	Convection coefficient $\bar{h}$	3 W/m^2K
Heat conduction k	398 W/mK	Environment temperature T_∞	25°C
Frequency f	15Hz	Current I_{RMS}	1354 A

Table 5: present working conditions

Busbars resistance value from [2].

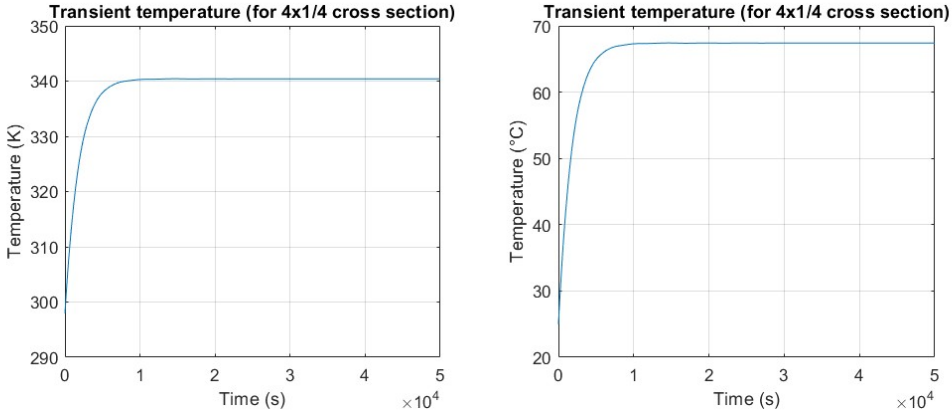

Figure 16: Heating up temperature transient, in Kelvin (left) and Celsius degrees (right)

The final steady state temperature is 67.4°C, with a ΔT_{rise} of 42.4°C.

PIP-II conditions, 4x1/4"
Table 6 summaries the conditions of the analysis, while figure 17 shows the evolution of the temperature of the bus bars $T(t)$.

b	4"	R	161.79 $\mu\Omega$
h	$\frac{1}{4}$"	ε	0.95
L	20'	$\bar{h}$	3 W/m^2K
k	398 W/mK	T_∞	25°C
f	20Hz	I_{RMS}	1695 A

Table 6: PIP-II working conditions

The final steady state temperature is 87.9°C, with a ΔT_{rise} of 62.9°C .

PIP-II conditions, 5x3/8"
Table 7 summarizes the conditions of the analysis, while figure 18 shows the evolution of the temperature of the bus bars $T(t)$.
Busbars resistance value from [2]. The final steady state temperature is 53.5°C, with a ΔT_{rise} of 28.5°C.

Conclusions.
This highly approximated lumped model gives an estimate of what the average temperature of the bus bars is going to be, neglecting thermal gradients- the Biot number suggests that the temperature is going to be uniform on the cross section, but it is not going to be uniform along

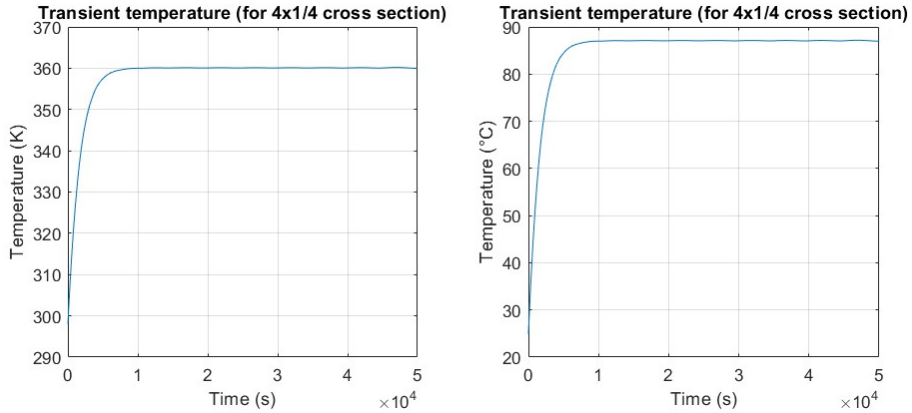

Figure 17: Heating up temperature transient, in Kelvin (left) and Celsius degrees (right)

b	5”	R	84.696 $\mu\Omega$
h	$\frac{3}{8}$”	ε	0.95
L	20’	$\bar{h}$	3 W/m^2K
k	398 W/mK	T_∞	25°C
f	20Hz	I_{RMS}	1695 A

Table 7: present working conditions

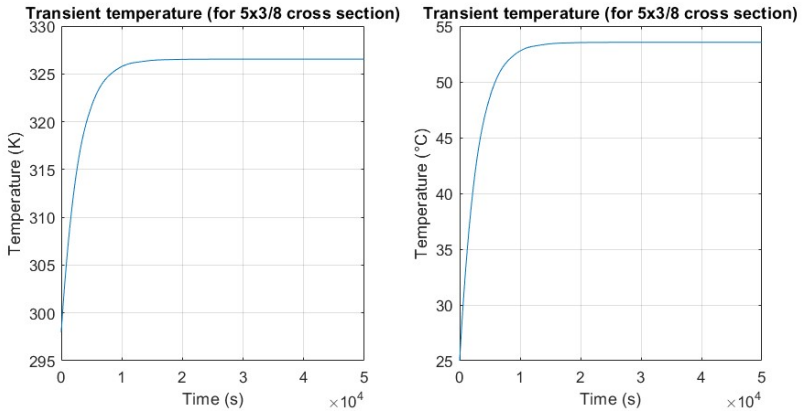

Figure 18: Heating up temperature transient, in Kelvin (left) and Celsius degrees (right)

the length of the conductor, and this is an important information that will need to be investigated with multi-dimensional calculations.

This analysis, however, has been useful to compare its highly approximated results with the expectations of the ampacity tables and to get an initial, quick estimate of the rise in temperature of the busbars in the actual working conditions.

2.2 2D COMSOL simulations

COMSOL Multiphysics is a finite element analysis and simulation software. It is particularly useful for modeling multiphysics systems, i.e. the bus bars discussed in this report, since their working conditions involve heat transfer and electrical phenomena.

The workflow is composed of the following fundamental steps:

- Geometry definition;

Figure 19: COMSOL Multiphysics logo

- Materials;
- Physics and boundary conditions;
- Creating the mesh;
- Study definition (i.e. stationary, time-dependent...)

In this section 2D simulations will be presented- the idea behind this step of the work is adding more complexity to the model one step at the time, making sure that the results keep going in the expected direction.

2.2.1 Ampacity table comparison

For starting, 2D simulations of the cross section in open air will be made to check if the results match with the analytical calculations presented in the previous section in the same conditions.

The single 4x1/4" bus bar is modeled as a simple rectangle, with a convective and radiative boundary condition. The heat source, in the 2D case, is not modeled from the current flow (because that would make it a 3D geometry) but as internal heat generation: Q_{joule}/V, where $Q_{joule} = \rho A/L \cdot I^2$.

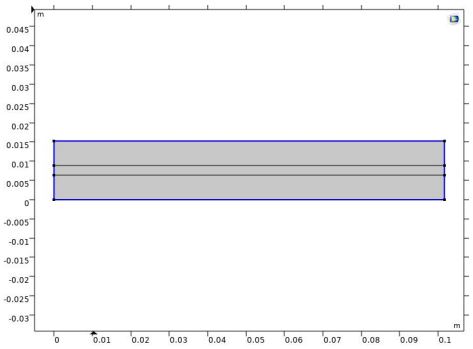

Figure 20: Boundaries for radiative and convective conditions

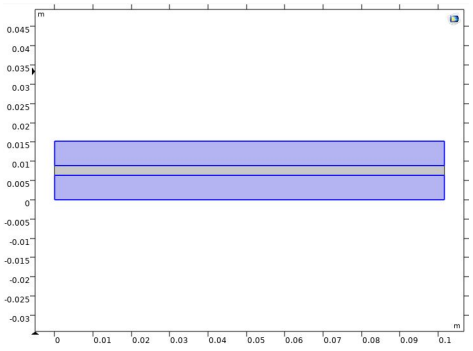

Figure 21: heat generation

Boundary conditions as specified on the ampacity tables:

- Ambient temperature 313.15K
- Surface-to-Ambient radiation with an emissivity of $\varepsilon = 0.4$

- Heat Flux (convection $h = 3W/m^2K$).
- Heat Source, defined as W/m^3.

Cross section	no. of busbars	I_{RMS}	T_{steady}	ΔT_{rise}
4x1/4”	single	1250 A	71.3°C	31.3°C
4x1/4”	single	1700 A	94.7°C	54.7°C
4x1/4”	single	1950 A	109.4°C	69.4°C
5x3/8”	single	1800 A	67.6°C	27.6°C
5x3/8”	single	2400 A	86.8°C	46.8°C
5x3/8”	single	2800 A	101.4°C	61.4°C

Table 8: Summary of 2D simulations results

Figure 22 shows an example of the results of the simulation. These results will be compared in the next section with the other analytical and numerical results in the same conditions.

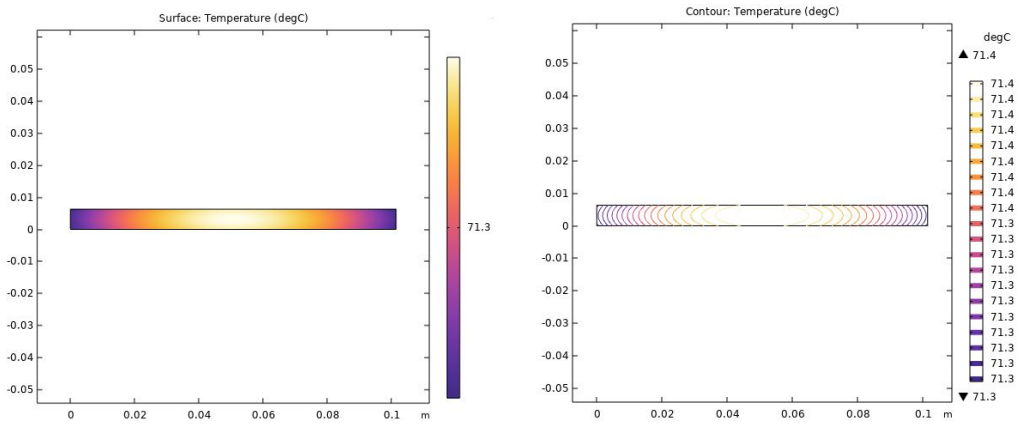

Figure 22: $I = 1250A$, $T_{steady} = 71.4$°C

Observations:

- The results of the simulations agree with the MATLAB calculations;
- The temperature of the cross section is uniform, as predicted from the Biot number.

2D simulations have been computed only for comparison with the ampacity table dataset and the comparison can be seen in figure 23. The choice to move forward with the complexity of 3D simulations has been made mainly due to the need of modeling the heat generation caused by the joule effect and see how the temperature increases in different parts of the length of the conductors.

2.3 3D COMSOL simulations

2.3.1 Ampacity table comparison

Running 3D simulation in the same conditions described in the ampacity tables gives overall the same steady state average temperature. Table 9 summarizes the results and figure 23 shows the comparison between the different sets of data- it can be clearly seen how 2D simulations agree with the analytical calculations, while 3D results show a small offset, which can be considered negligible.

For these simulations two physics modules have been added to the simulation, in order to model the Joule effect: the heat transfer module and the electric current module. The two modules can be coupled to obtain electromagnetic heating (joule effect). An important detail to keep in mind is that the electric current module must be defined only on the two conductors.

Cross section	no. of busbars	I_{RMS}	T_{steady}	ΔT_{rise}
4x1/4”	single	1250 A	70.07°C	30.07°C
4x1/4”	single	1700 A	92.62°C	52.62°C
4x1/4”	single	1950 A	106.8°C	66.8°C
5x3/8”	single	1800 A	66.52°C	26.52°C
5x3/8”	single	2400 A	85.06°C	45.06°C
5x3/8”	single	2800 A	99.21°C	59.21°C

Table 9: Summary of 3D simulations for comparison with the ampacity table

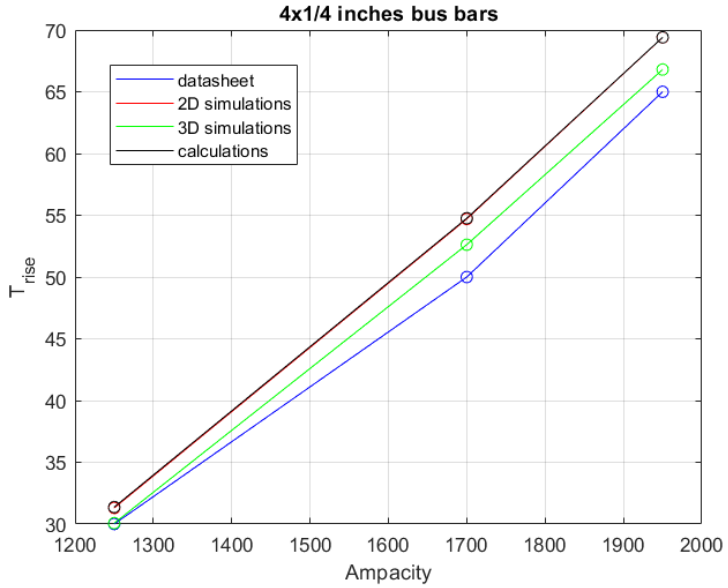

Figure 23: Ampacity table comparison for 4x1/4”

Figure 24 shows the temperature plot of a single bus bar- compared to 2D simulations there is a stronger effect of the extremities because the lateral surface area is larger, as expected.

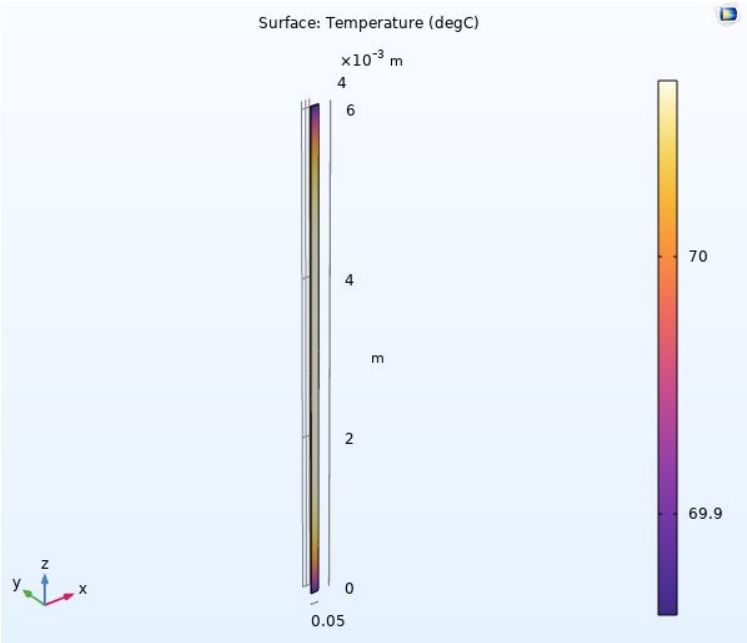

Figure 24: Simulation of 4x1/4” 20’ busbar, 1250A, 40°C, $\bar{h} = 3W/(m^2K)$

Calculation of the convective coefficient
Altough this aspect has been neglected in the lumped capacity and 2D analysis, it must be kept in mind that natural convection is affected by the temperature of both the ambient air and the surface of the component- so it is possible to use experimental correlations between adimensional numbers to estimate h from the Nusselt number, at different temperatures.
The **Nusselt number** is the ratio of convective to conductive heat transfer at a boundary in a fluid and it can be used to calculate h:

$$Nu = \frac{h\delta}{k} \tag{7}$$

Natural convection is described by **Grashof number**, a dimensionless group that represents the ratio of the buoyancy force to the viscous force acting on the fluid.

$$Gr = \frac{g\Delta T\beta\delta^3}{\nu^2} \tag{8}$$

where g in the gravitational acceleration, $\Delta T = T_s - T_\infty$ the difference between the surface temperature and the fluid temperature, δ is a characteristic length of the geometry and ν is the kinematic viscosity of the fluid.

The **Prandtl number** is defined as the ratio of momentum diffusivity to thermal diffusivity.

$$Pr = \frac{\nu}{\alpha} \tag{9}$$

The **Rayleigh number** is defined as the product of the Grashof and Prandtl number. If $Ra < 10^9$ the flow can be considered laminar, otherwise the flow is turbulent.

$$Ra = Pr \cdot Gr \tag{10}$$

Rayleigh number is related to the Nusselt number with experimental correlations that follow an exponential law: $Nu = C \cdot Ra^n$, where the constants C and n depend on the geometry of the surface and the flow. Approximating the bus bas assembly as a vertical plate, the correlations for laminar and turbolent flow are the following:

$$Nu = \begin{cases} 0.59Ra^{\frac{1}{4}} & \text{if } Ra \in [10^4, 10^9] \\ 0.1Ra^{\frac{1}{3}} & \text{if } Ra \in [10^9, 10^{13}] \end{cases}$$

Once the Nusselt number is calculated, it is possible to reverse equation 7 to obtain h.

The properties of air at ambient temperature are from 'The Engineering Toolbox' website (reference [6]). Table 10 shows an example of the calculations.

Ambient temperature T_∞	25	°C
Surface temperature T_s	80	°C
Film temperature T_m	$(T_\infty - T_s)/2$	°C
Prandtl number Pr	0.707	
β	$1/T_m$	$1/K$
Characteristic length L	20	ft
Thermal conductivity k	0.02624	$W/(m^2K)$
Grashof number Gr	$1.559 \cdot 10^{12}$	
Rayleigh number Ra	$1.102 \cdot 10^{12}$	
Nusselt number Nu	$1.033 \cdot 10^3$	
Convection coefficient h	4.446	$W/(m^2K)$

Table 10: Data and calculations for the convection coefficient

2.3.2 Present working conditions

In this section, the results of the simulation for the present working conditions will be described. This simulation shows the full bus bars assembly and the materials surrounding it, and will be used for a comparison with experimental data, necessary to validate the model.

Figures 25 and 26 show the geometry of the model. As seen in figure 25, the bus bars is 22 feet long, of which 20 feet are inside the penetration and 2 and exposed to air (forced convection) in the booster tunnel. Of the 20 feet inside the penetration (which has been modeled as vertical, in the simulations), 10 feet are exposed to air (natural convection) and the last 10 feet are wrapped in the neutron shield, made of polyethylene beads.

Lastly, there are two point underlined in figure 25, named as 'upper' and 'lower'. They represent the actual placement of two **thermocouples** that have been used to gather experimental data. This is important for the validation of the model and will be discussed later in this report.

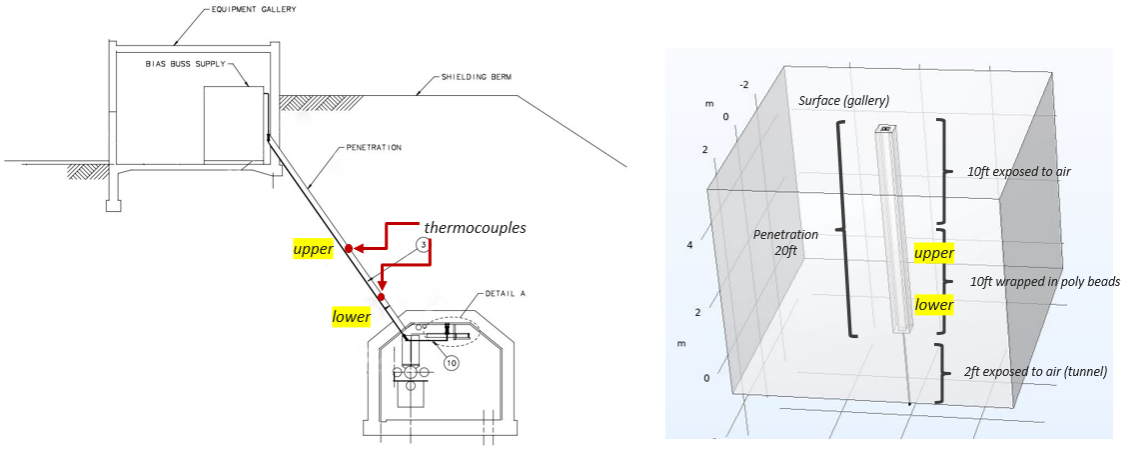

Figure 25: 3D geometry of the model

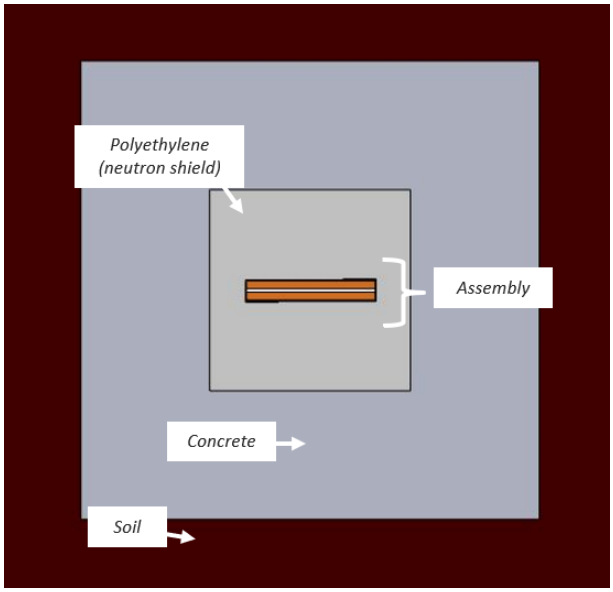

Figure 26: Cross section of the geometry

The technical drawing the of bus bars assembly can be seen in figure 27.

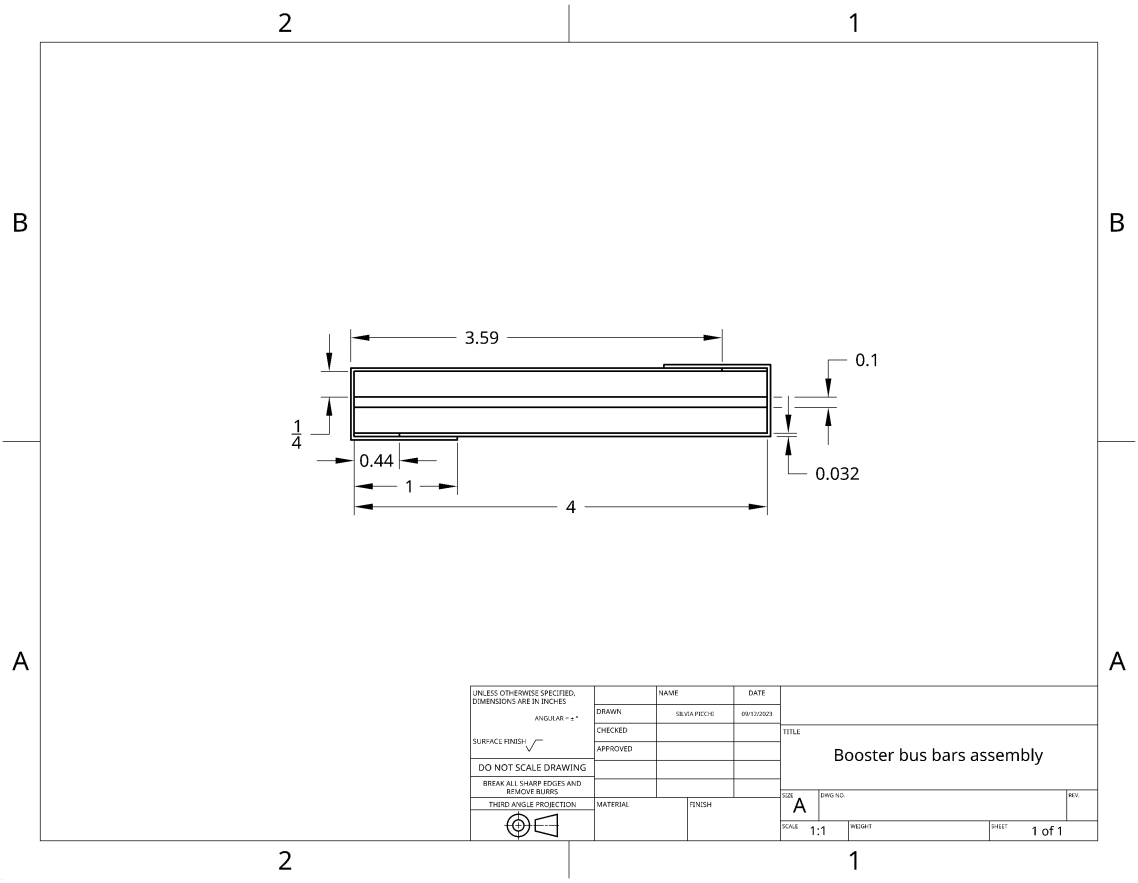

Figure 27: Technical drawing of the bus bars assembly

After the definition of the geometry, the simulations needs the properties of the materials and the boundary conditions (which can be briefly seen in figure 28).

Figure 28: Boundary conditions

Tuning. This section addresses the method that has been used to move forward with the analysis in the cases when there was no information available about a parameter. An example of this would be the thermal conductivity of the soil (which is variable with temperature and moisture) and the exact thickness of the concrete layer surrounding the assembly.
A way around this problem is to perform a **parametric sweep**, that is computing a simulation for a range of plausible values of a parameter, and then choosing the results closer to the expectations. This kind of **tuning the model to experimental data** can be necessary in this cases, but needs to be used as little as possible.

Figure 29 shows an example of a parametric sweep for the conductivity of the soil. The graph shows the temperature along the middle line of a bus bar for different value of the thermal conductivity.

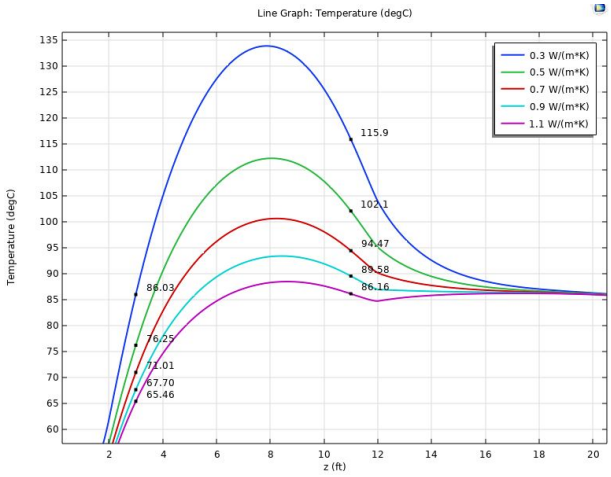

Figure 29: Example of a parametric sweep

Results. Figure 30 shows the results of the simulations:

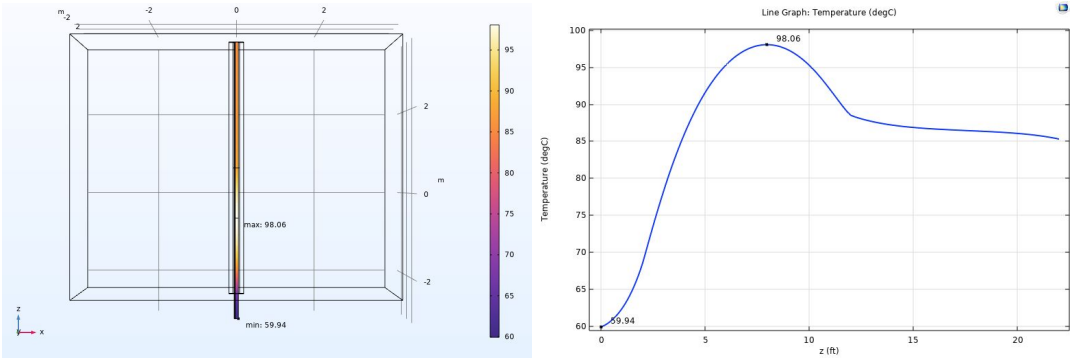

Figure 30: Simulation results for present working conditions

On the left, figure 30 shows the 3D temperature distribution on the busbars surface. On the right, it is possible to see how the temperature varies along the middle line of a single bus bar. As expected, from right (22ft, gallery surface) to left (0ft, tunnel), the temperature rises until it reaches a maximum where the bar is surrounded by the polyethylene beads (since it works also as thermal insulation) and then decreases rapidly due to the forced convection and water cooling in the tunnel.

Qualitatively, the temperature distribution reflects the expectations. These results need also to be compared with experimental data in order to understand whether the model is reliable or not.

Model validation. There are many checks and comparisons that can be made to validate the model.

The first, easiest kind of validation is performing an **energy balance** of the model. It can be rather common for thermal simulations to show sensible results, but actually have some errors in the boundary conditions which lead to the violation of the conservation of total energy. From the first law of thermodynamics, the well-known global heat balance equation can be derived:

$$\frac{dE_{tot}}{dt} = -\sum_{k=1}^{n} \dot{m}_k h_k + \sum_{i=1}^{m} \dot{Q}_i - \dot{L}_n \tag{11}$$

Since this is a steady-state simulation, with no mass flow and no net work, the only term of the balance is the heat flux $\sum \dot{Q}$.
These terms can be easily evaluated once the simulation is computed. The balance equation written using the predefined variables in COMSOL Multiphysics becomes:

$$\text{ht.dEi0Int + ht.ntefluxInt - ht.QInt = 0}$$

At steady state, the total accumulated energy rate is zero. The total net energy rate and the total heat source must balance (even with a small tolerance- see figure 31).

Total heat source (W)	Total accumulated energy rate (W)	Total net heat rate (W)	Energy balance (stationary) (W)
625.44	0.0000	625.04	-0.39563

Figure 31: Energy balance

Once it is proved that the simulations does not have any intrinsic error, it is possible to **compare the experimental data and the simulations results**. The data reading correspond to the two thermocouples described with the geometry of the model, named *'upper'* and *'lower'*.

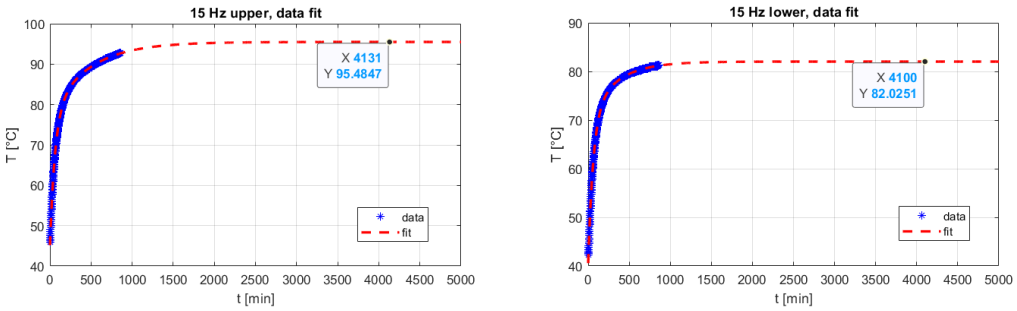

Figure 32: Thermocouples readings with data fitting

Figure 32 shows how at steady-state the upper thermocouple would reach about 95°C while the lower thermocouple would reach about 82°C. The simulations results can be seen in figure 33- highlighted in the figure are temperatures at 1-2 feet from the top and the bottom of the section wrapped in polyethylene, to be compared with experimental data. They show a value of 92-95°C for the upper and 78-86°C for the lower thermocouple. In this case, experimental data is compared to a range of values and not with the temperature of an exact point (the placement of the thermocouples, which is known) to take into consideration the uncertainties of the model, which have been briefly discussed in the tuning section. It is reasonable to expect that experimental and simulated data will not match point by point, but rather that the simulation will be able to give a good estimate of the temperature in a point and model effectively the temperature gradients.

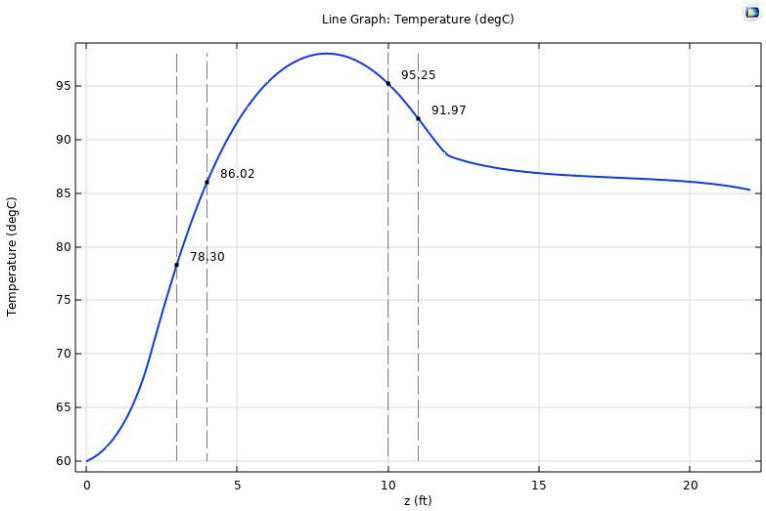

Figure 33: Simulation results

This comparison allows to say that experimental data and simulation data in the analyzed surface match.

Lastly, another comparison can be made with thermal imaging. An IR camera has been used to evaluate the temperature of the bus bars as they reach the tunnel and come out from the bottom of the penetration, as can be see in figure 34.
The temperature measured by the IR camera is 71.2°C, while the simulation shows a value of 68.7°C, which is close enough (error 3,5%) to say that the results match.

Figure 34: Thermal imaging of the busbars (71,2°C). © Victor Grzelak, Fermilab

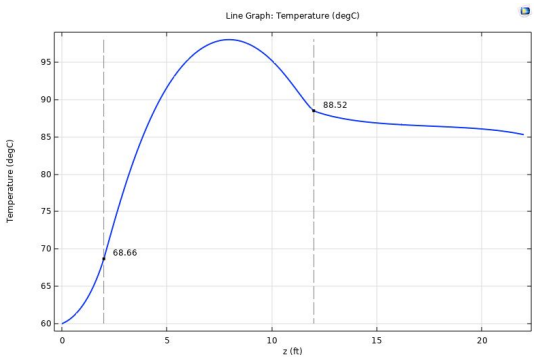

Figure 35: Simulation results

2.3.3 PIP-II working conditions, present assembly

This section presents the results of the simulations of the system in future PIP-II working conditions, without making any changes to the assembly. The only difference form this simulation and the previous is the current level (1695A RMS), so, since the previous simulation proved to be in accordance with experimental data, the results of this simulation can be regarded as reliable as well.
The most important thing to underline is that, according to these results, **the polyethylene neutron shield will reach melting temperature** ($T \geq 126$°C), so **this system will not work safely in these conditions** (see figures 36 and 37). The model does not take into consideration the melting of the material, so any simulation that goes above the melting temperature will not show the actual conditions.

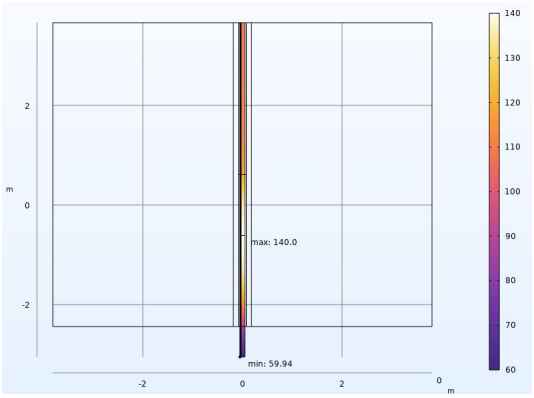

Figure 36: Temperature distribution on the bus bars

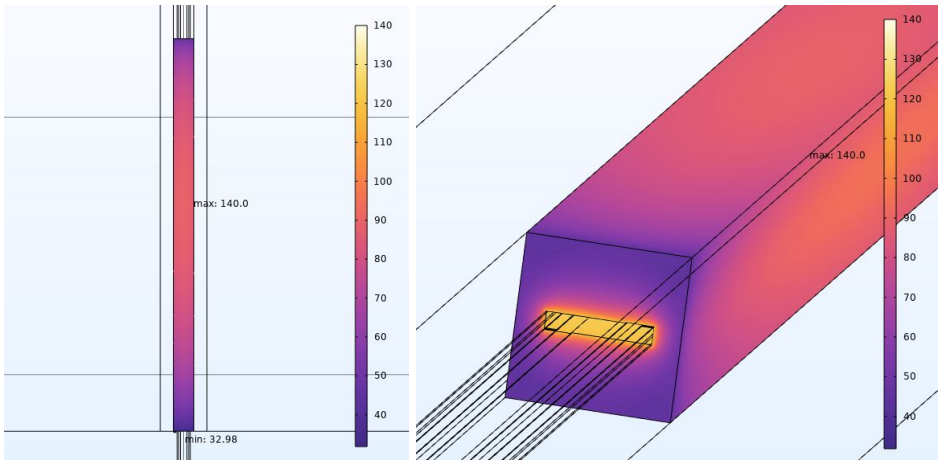

Figure 37: Temperature distribution on the polyethylene shield

However, this simulation is useful because it confirms something that has only partially been evaluated by experimental tests- that the infrastructure needs to be improved.

The temperature in these conditions has been measured during a test in station 12 which was supposed to last three days, but was shut down after a few hours due to an excessive rise in temperature, so the test did not reach steady-state conditions. The thermocouples were placed in the same spots described in the previous section (upper and lower).
Figure 38 shows the comparison between the available experimental data and the results of a **transient simulation**- the initial trends of the curves agree, even though experimental data shows a steeper slope. This might be due to the fact that the simulations only take into consideration a constant RMS current, while the actual current curve as a function of time (as seen in figure 7) can cause the transient curve to be different.

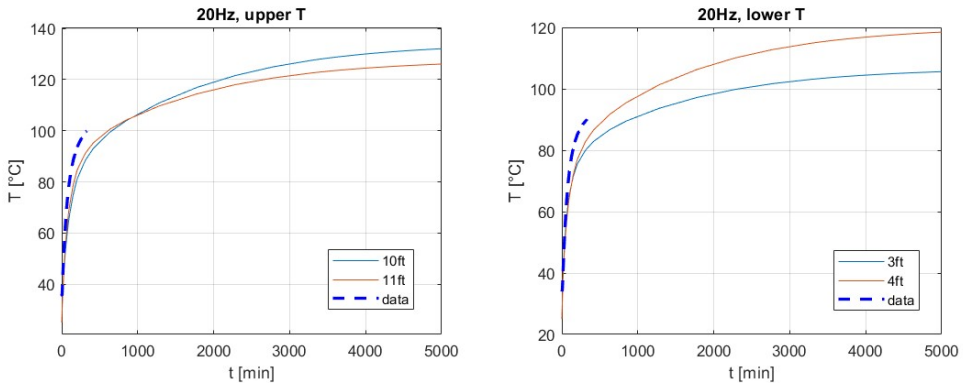

Figure 38: Temperature distribution on the polyethylene shield

Figure 39 shows the steady-state temperatures in the upper and lower points that the assembly would reach if the melting of the polyethylene beads (which will inevitably change the actual results) could be neglected.
Figure 40 shows the maximum and minimum temperatures reached in these conditions. Once again, the result to underline is that the maximum temperature is going to be well above the melting temperature of the neutron shield, so it is safe to safe that it will melt, even taking into consideration the uncertainties of the simulations.

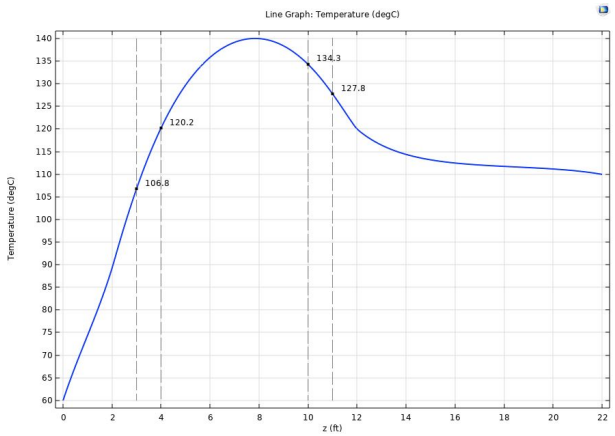

Figure 39: Steady-state temperatures (upper-lower thermocouples)

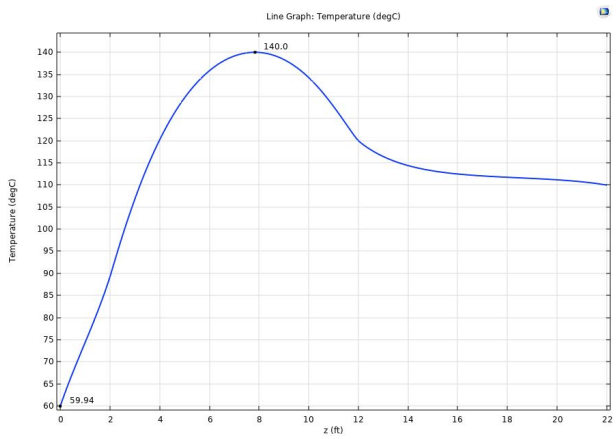

Figure 40: Steady-state temperatures (maximum and minimum)

2.3.4 PIP-II working conditions, new assembly

This section presents the results of the simulations of the assembly in future PIP-II working conditions, with an increased cross section of the conductors. As already discussed, a bigger cross section will cause a decrease in the resistance and a bigger heat capacity due to bigger mass.

Figure 41 shows the technical drawing of the cross section of the new assembly. The rest of the geometry is exactly the same as previously described.

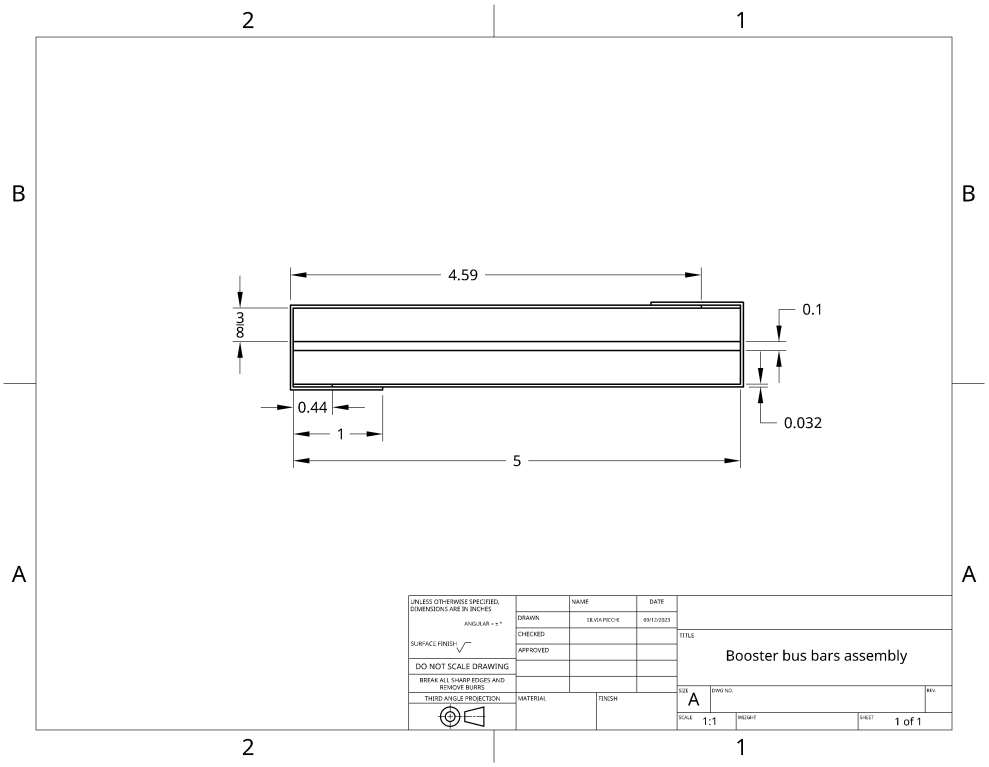

Figure 41: 5x3/8" cross section

Figures 42 and 43 show the temperature distribution in the bus bars and in the poly-beads. These simulations cannot be compared to actual experimental data, but the results look promising- the temperatures are not only below the melting point, but are also lower than the ones reached in present working conditions.

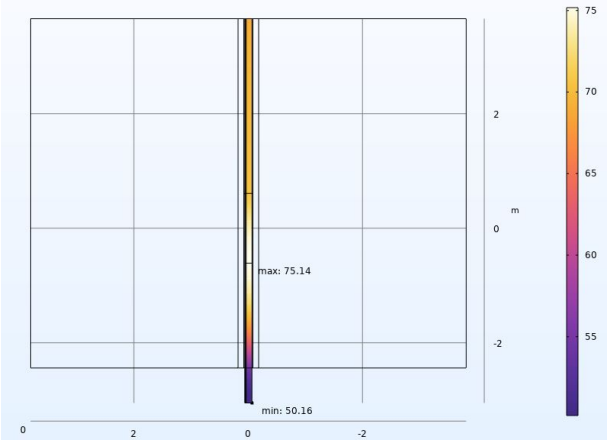

Figure 42: Temperature distribution on the bus bars

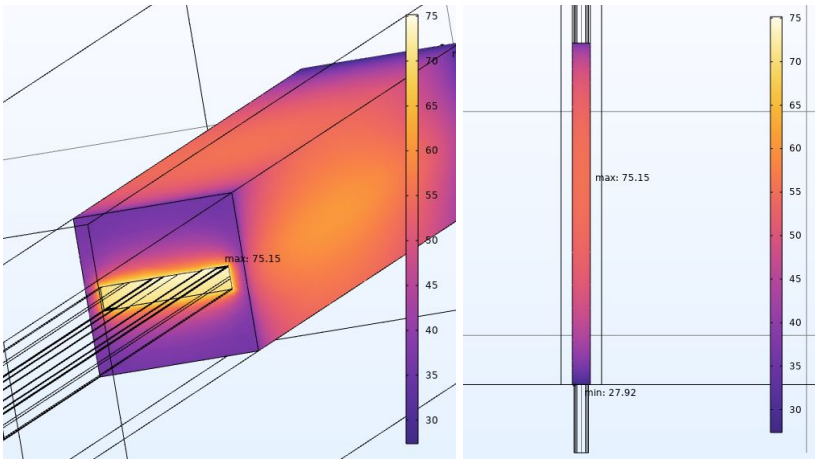

Figure 43: Temperature distribution on the polyethylene shield

For comparison, figures 44 and 45 show the temperature along the surface of the assembly, highlighting the upper and lower thermocouples range and the maximum/minimum value.

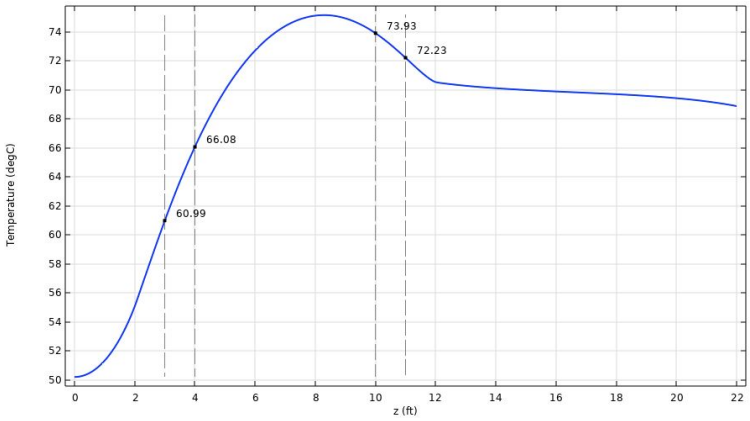

Figure 44: Steady-state temperatures (upper-lower thermocouples)

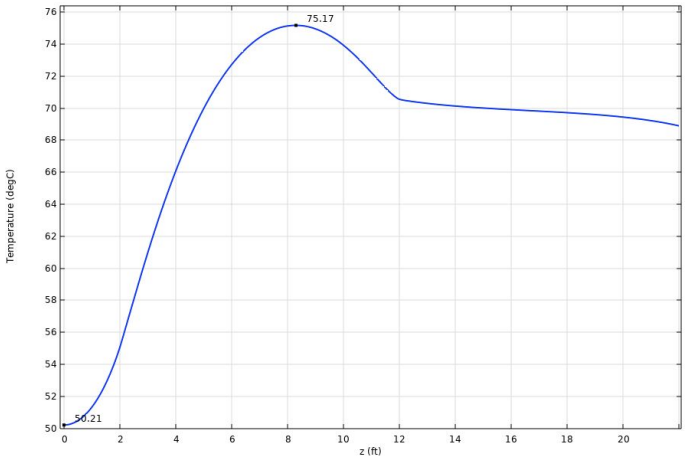

Figure 45: Steady-state temperatures (maximum and minimum)

2.3.5 Results

Table 11 summarizes the results of 3D steady state simulations computed for different working conditions, described in the previous sections.
These results briefly show how increasing the current with the same infrastructure will cause the temperature to be too high, while increasing the cross section of the bus bars would restore safe operational temperatures.

Changing the cross section is only one of the many possible solutions to the thermal problem. It is effective, because the expected temperatures are much lower than the previous ones, but it might not be the optimal solution. Not only changing the cross section of the assembly, for the 22 stations, would mean a lot of work (as would be, for example, designing and implementing and air cooling or water cooling system), but most importantly it would not address the root of the problem, that is the current. An optimal solution to the problem would be **reducing the RMS value of the bias current**, which would mean **less heat dissipation** (and thus a more energy-efficient system) and consequently **lower temperatures** and **lower gradients**.
A way to do so would be, for example, changing the harmonic number of the accelerator or, more realistically, through a redesign of the ferrite tuner, in order to make them work in the same way at lower RMS currents. Section 3 presents an analysis of the implications of a different harmonic number.

Table 12 shows the change of the temperature gradient for the present cross section (4x1/4"), between the point at the bottom of the penetration (2ft, in the frame of reference of the COMSOL model) and the point of maximum temperature. As expected, lower currents also generate lower thermal gradients.

	Present	PIP-II	
Conditions	1354A, 4x1/4"	1695A, 4x1/4"	1695A, 5x3/8"
T_{max}	98.06°C	140.0°C	75.15°C
T @3ft	78.30°C	106.8°C	60.99°C
T @4ft	86.02°C	120.2°C	66.08°C
T @10ft	95.25°C	134.3°C	73.93°C
T @11ft	88.52°C	127.8°C	72.23°C
T_{avg} bus bars	86.49°C	116.15°C	68.40°C
T_{avg} clampshell	86.48°C	116.13°C	68.39°C
T_{avg} polybeads	70.4°C	94.9°C	58.17°C
Energy balance	-0.4W	-0.7W	+1.6W

Table 11: Summary of 3D steady state results

Current [A]	1250	1500	1750	2000
Gradient [K/m]	13.3	21.9	30.9	42.7
Gradient [K/ft]	4.05	6.67	9.43	13.0

Table 12: Thermal gradients for different current level

2.4 Peak temperature tables

The 3D simulations previously presented can be useful in many ways. An example would be using them to build an ampacity table, or more precisely, a **peak temperature table**- this powerful tool has been discussed and used widely in the first part of this work in order to validate the model later expanded and modified.
This table is document that allows to predict the temperature rise of the bus bars assembly as a function of the RMS current that the conductors bring to the cavities.

In this section two peak temperature tables will be presented, for 4x1/4" and for 5x3/8" cross sections. A few details to keep in mind when using these tables:

- The temperature rise ΔT_{rise} is defined as the difference in temperature between the ambient temperature (assumed to be $T_{amb} = 25°C$) and the maximum temperature of the assembly T_{max}. This choice was made thinking that the maximum value of the temperature would be more significant than the average temperature of the assembly.

- If the ΔT_{rise} is defined for the surface temperature of the assembly in the part exposed to air, instead of a temperature in the part wrapped in polybeads, then the convection coefficient must be evaluated for each current value, since it affects directly (and it is affected by) the surface temperature.

  In this case, since the focus is on a surface not exposed to natural convection, the variations of h have been neglected.

2.4.1 Data analysis

In order to write the tables, 3D simulations have been computed with a parametric sweep on the current value. An example can be seen in figure 46, which shows the variations in temperature rise along the length of the assembly, with an highlight on the maximum temperature and the uniform temperature in the portion of the bars not surrounded by the shield.
This kind of parametric sweep takes quite some time to compute (about an hour).

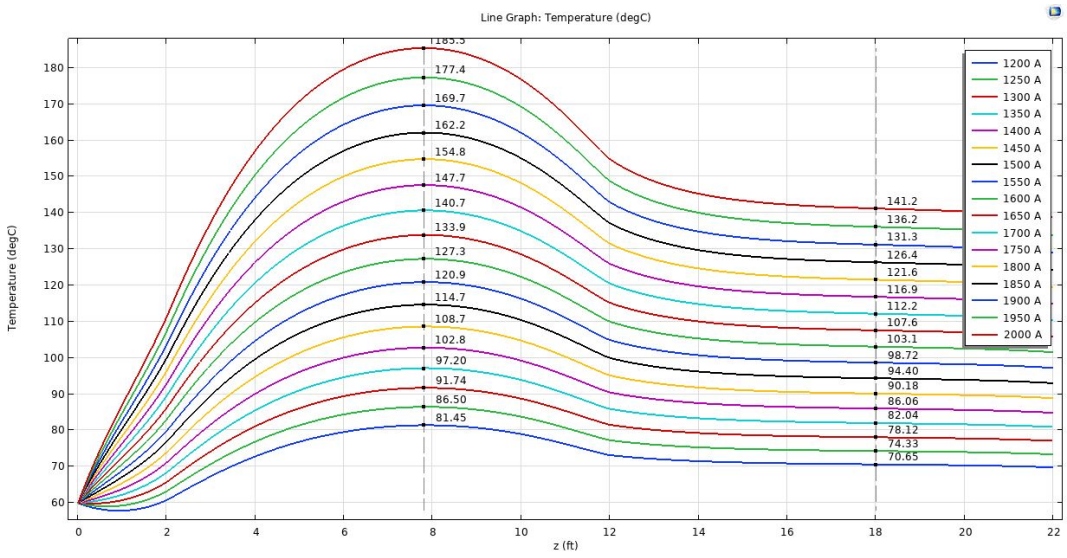

Figure 46: Example of current sweep on the 4x1/4" assembly

Figure 47 shows the **maximum temperature** of the **4x1/4" assembly** as a function of the current. The data can be fitted with a quadratic curve to interpolate all the intermediate values and to evaluate which current level gives a certain ΔT_{rise}, as seen in figure 49.

The same process described has been made for two cross sections: 4x1/4" and 5x3/8".
Figures 46 to 49 refer to the 4x1/4" assembly, while figures 50 to 52 refer to the 5x3/8" assembly.

4x1/4" graphs

The following figures show the process followed to obtain the tables for the 4x1/4" cross section.

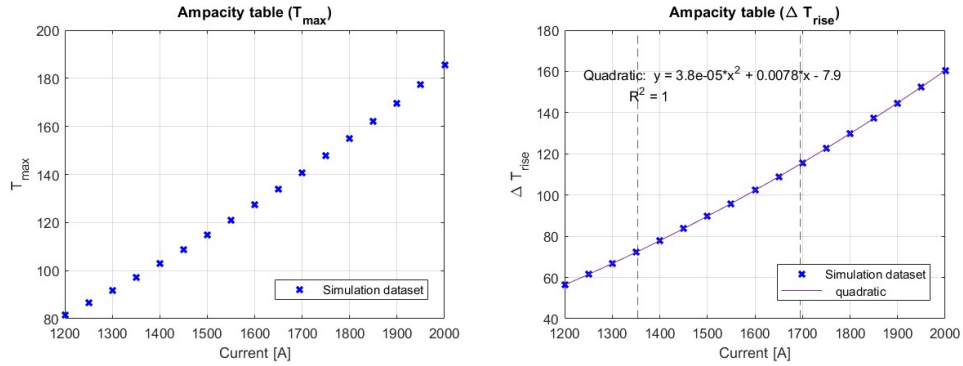

Figure 47: T (left) and ΔT_{rise} (right) as a function of the current

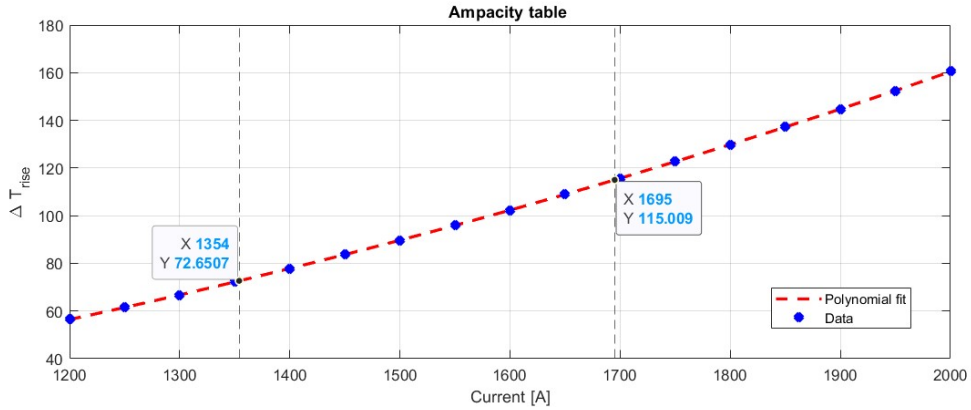

Figure 48: Highlight on the ΔT_{rise} expected for the working conditions

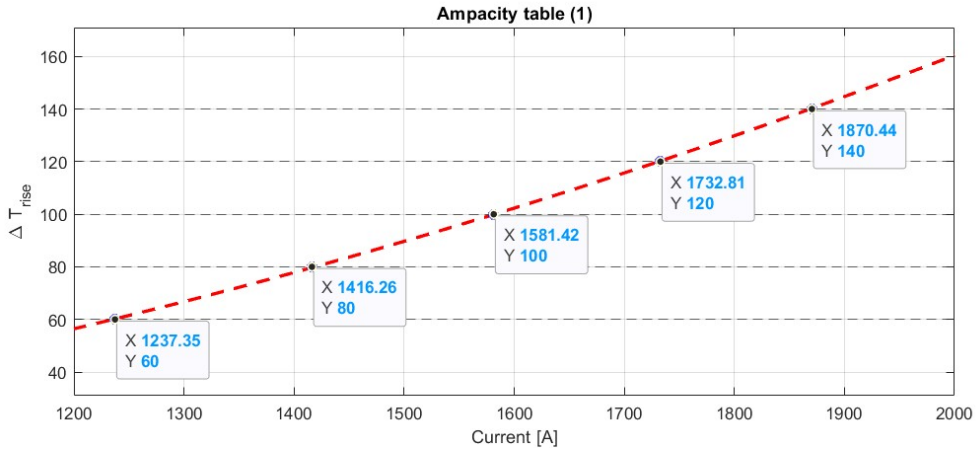

Figure 49: Ampacity table evaluation

5x3/8" graphs

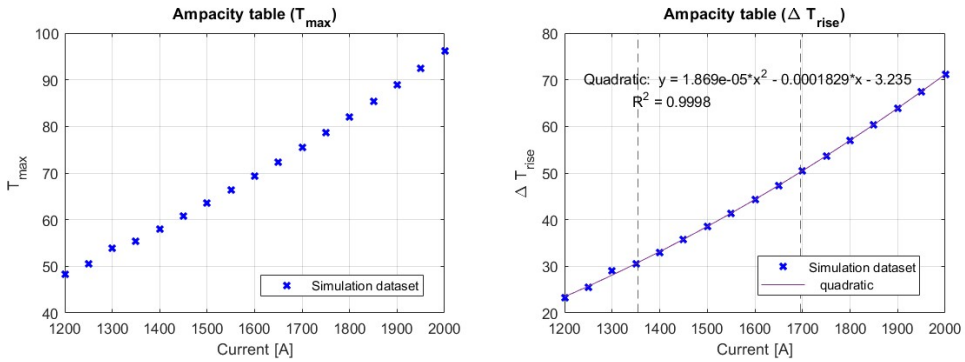

Figure 50: T (left) and ΔT_{rise} (right) as a function of the current

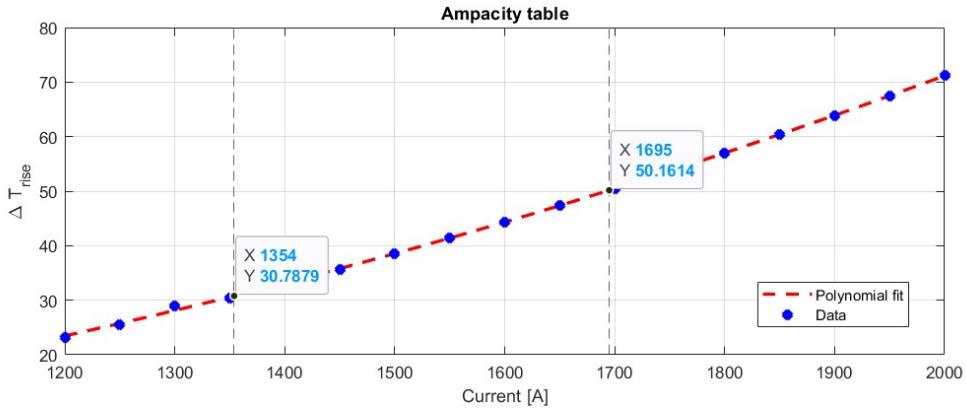

Figure 51: Highlight on the ΔT_{rise} expected for the working conditions

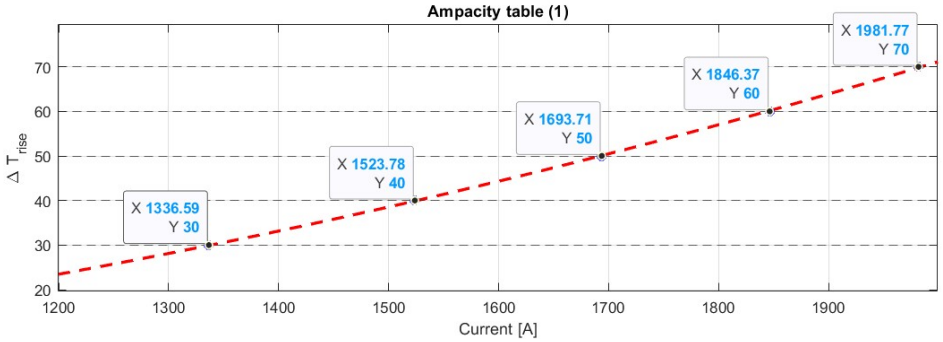

Figure 52: Ampacity table evaluation

2.4.2 Results

The results of the data analysis is summarized in tables 13, 14 and 15.

Section	Current	ΔT_{rise}
4x1/4”	1237 A	60°C
	1416 A	80°C
	1581 A	100°C
	1733 A	120°C
	1870 A	140°C

Table 13: Ampacity table for 4x1/4”

Section	Current	ΔT_{rise}
5x3/8”	1337 A	30°C
	1524 A	40°C
	1694 A	50°C
	1846 A	60°C
	1982 A	70°C

Table 14: Ampacity table for 5x3/8”

Table 15 can be useful in many cases, for example:

- for a quick evaluation of the maximum temperature reached by the assembly, in case the working condition need to be changed,
- for temperature evaluation in case of a future redesign of the ferrite tuners, which means that the system will work at a different RMS current.

.

Section	ΔT_{rise}					
	30°C	40°C	50°C	60°C	70°C	80°C
4x1/4”	943 A	1045 A	1143 A	1237 A	1329 A	1416 A
5x3/8”	1337 A	1524 A	1694 A	1846 A	1982 A	2010 A
” ”	ΔT_{rise}					
	90°C	100°C	110°C	120°C	130°C	140°C
4x1/4”	1501 A	1581 A	1686 A	1733 A	1803 A	1870A
5x3/8”	2208A	2284 A	2351 A	2400 A	2432 A	2446 A

Table 15: Summary

3 RF analysis

3.1 Radio Frequency Systems

Variables

$\vec{F}$	force	N
$\vec{E}$	Electric field	V/m
$\vec{B}$	Magnetic field	T
$\vec{v}$	velocity	m/s
q	electric charge	C
f	machine frequency	MHz
f_{RF}	RF frequency	MHz
f_{rev}	Revolution frequency	MHz
T_{rev}	Revolution period	μs
h	harmonic number	[-]
β		[-]
γ		[-]
c	light speed (c=1)	[-]
m_p	Proton mass	eV/c^2
E_{tot}	Total energy	eV
KE_{inj}	Injection kinetic energy	eV
KE_{ext}	Extraction kinetic energy	eV
p_i	Injection momentum	eV/c
p_e	Extraction momentum	eV/c
C	Booster circumference	m

3.1.1 Main concepts

Radio Frequency (RF) refers to the high-frequency electromagnetic fields that accelerate and manipulate charged particle beams. These fields resonate as standing waves in enclosed devices called "cavities," and oscillate quickly to push beam as it passes. The frequency of the field oscillation is usually in the radio portion of the electromagnetic spectrum, hence the term "Radio Frequency."

To understand how particle beams are accelerated, let us recall the *Lorentz force equation*:

$$\vec{F} = q(\vec{E} + \vec{v} \times \vec{B}) \tag{12}$$

A static magnetic field cannot increase the kinetic energy of the beam, because its force is always perpendicular to the particle velocity- this is why we use electric fields to increase particle kinetic energy in an accelerator.

Figure 53 illustrates the electric and magnetic forces on a moving charged particle. While the magnetic force must be perpendicular to the magnetic field and the particle velocity, the electric force has no such limitation. Thus we can choose an electric field direction such that the electric force points parallel to the particle velocity.

In short, the concept is that **an electric field accelerates the beam**, while **the magnetic field bends it**.

High-frequency electromagnetic fields, instead of magnetic or electrostatic fields, are necessary to accelerate the beam. It is infeasible to use static electric fields in high-energy accelerators, because the necessary high voltages would cause electrostatic breakdown and arcing; instead, most modern high-energy accelerators use hollow conducting structures known as **RF cavities** that contain electromagnetic waves. These cavities are **electromagnetically resonant**, in that they efficiently store oscillating energy at particular frequencies.

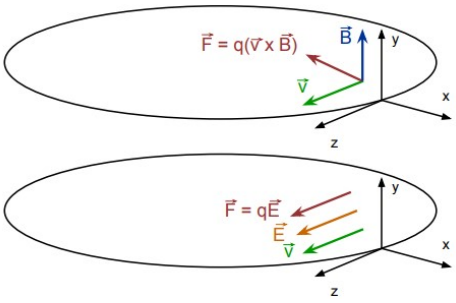

Figure 53: Electric vs. magnetic force on a charged particle.

Fermilab's RF cavities use standing waves generated from the interference between traveling and reflected waves inside the cavity. A standing wave doesn't appear to move through the cavity, because only the amplitude of the wave oscillates. Figure 54 shows a model of a simple RF cavity, known as a "pillbox cavity." The magnetic and electric fields are shown at a particular point in the cycle, but the field amplitudes actually oscillate in time at high frequency (as shown in figure 55).

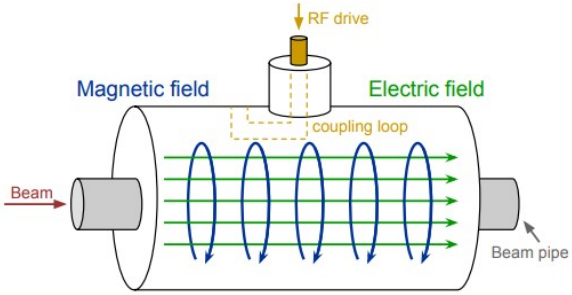

Figure 54: Simple RF 'pillbox' cavity

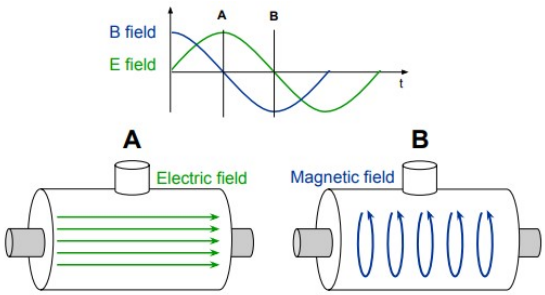

Figure 55: Timing difference between magnetic and electric fields.

RF cavities must be very efficient oscillators to keep power loss as low as possible and to maximize the field delivered to the beam. However, this means that they only work at frequencies very close to their resonance. For **synchrotrons**, where **the RF frequency increases throughout the acceleration process**, we must be able to change the resonant frequency of the RF cavity as needed.

3.1.2 RF cavity Q and Ferrite Bias Tuning

The **quality factor** or "Q" provides a quantitative definition of the energy efficiency of an oscillator, and is defined as the resonant frequency f_{RF} multiplied by the ratio of stored energy to lost power:

$$Q = 2\pi f_{RF} \frac{energy stored}{power lost} \tag{13}$$

This alternative expression for Q shows how this is related to the frequency width of the cavity response:

$$Q = \frac{f_{RF}}{\Delta f} \tag{14}$$

This equation means that **high-Q resonators** like RF cavities have a narrow frequency response- they resonate efficiently in a very limited frequency range, as shown in figure 56. Trying to drive an RF cavity at a frequency that is not close to its resonance, will result in taking much more power to achieve a strong field.

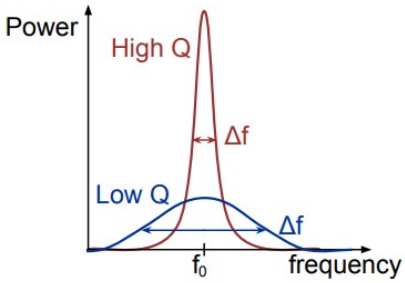

Figure 56: Resonator quality factor, high vs. low Q

This trade-off between power efficiency and narrow frequency range is acceptable for linear accelerators (such as PIP-II), where the cavity frequency does not change. However, synchrotrons require the RF frequency to increase with the beam energy, so we must have a way of changing the resonant frequency of the cavities. In the Main Injector and Booster, we accomplish this by attaching small coaxial RF transmission lines to the RF cavities that are loaded with ferromagnetic material, called **ferrite tuners**. They are coupled to the cavity, so they become part of the resonating volume.

It is possible to create a biasing field that changes the magnetic permeability of the ferrite by applying a large amount of current, usually several thousand amps, through the center of the tuner. By changing the permeability of the ferrite, it is possible to **change the inductance of the resonant volume** in the cavity and tuner.

Therefore, by changing the biasing current applied to the tuners, it is possible to actively control the resonant frequency of the entire RF cavity, which allows for the changing RF frequency needed in a synchrotron.

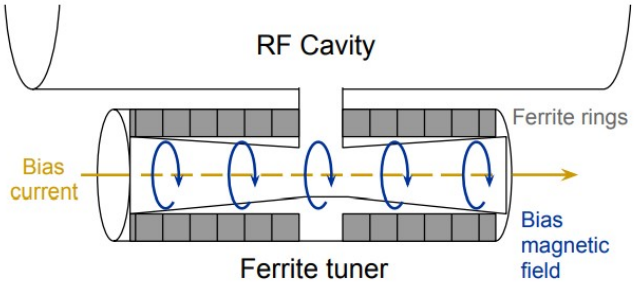

Figure 57: RF cavity with attached ferrite tuner

3.1.3 RF Phase and Synchronicity

The RF oscillations must match precisely with the periodic arrival of beam in the cavity to achieve stable acceleration. Since the cavity's fields oscillate in time, their force direction changes throughout the cycle- and even though the electric field is parallel to the beam velocity, it points in the opposite direction during half the cycle. Thus the timing of the RF oscillations must match with the arrival of particles so they only see the electric field when it is pointing forward.

Particle arrival time with respect to the RF cycle is known as the **RF phase**. For this to occur, the following relationship must be met between the RF frequency f_{RF}, the distance between cavities L, and the particle velocity v, and integer n:

$$f_{RF}L = nv \tag{15}$$

The particles that meet the **synchronicity condition** are known as the **synchronous particles**, and they receive the correct energy increase from the RF as per the design of the accelerator. The phase at which the synchronous particle arrives in the cavity is known as the **synchronous phase**, and provides a reference point in RF system timing.

As the particle velocity increases, the product $f_{RF}L$ must increase to maintain synchronicity. For a linear accelerator like PIP-II, the distance between accelerating cavities L progressively increases to follow the increase in particle momentum. However, circular accelerators use successive passes through the same RF cavities to accelerate beam, and this means that the RF frequency f_{RF} needs to increase to keep pace with the accelerating beam particles.

3.1.4 Phase Focusing and Stability

Beam particles in a group do not all have the exact same momentum, and the RF must be able to maintain particle stability even with these small perturbations.

Because of this momentum spread, each particle arrives in the cavity at a slightly different time, which corresponds to different points along the RF waveform. Thus, each particle will experience a different electric field strength and, by controlling the RF phase, we can provide a restoring force that encourages errant particles to move toward the momentum of the synchronous particle.

This longitudinally-focusing process is called **phase focusing**- it allows particles with momentum deviations to be corrected slightly with each pass through an RF cavity. This focusing ability of the RF has, however, some limitations.

The stable RF space that can phase focus the beam is referred to as the **bucket**. If a particle's energy and phase are within the bucket, then it can be phase focused into stable motion. The number of RF buckets in a machine is limited, because there are only so many RF oscillations in the time it takes a particle to make one orbit.

The number of RF buckets for a given synchrotron is called the **harmonic number**, which is equal to the number of RF oscillations per revolution period:

$$h = \frac{f_{RF}}{f_{rev}} \tag{16}$$

The Booster has been operated with a harmonic number of 84. This value can be considered arbitrary, in some way, but the Main Injector and Recycler require a specific injection frequency, forcing the Booster extraction frequency to match for bucket-to-bucket transfer- so in theory the harmonic number of the Booster can be changed (which will be object of discussion), but that modification implies changes in the other machines' working conditions, as well.

The phase focusing process causes beam to collect into **discrete packets**, known as **bunches**. Figure 64 shows the qualitative difference between unbunched (called "DC") beam, and beam bunched by interaction with the RF waveform.

Since the bucket area is the only stable place for beam to exist, it is often said that the bunches fill the buckets.

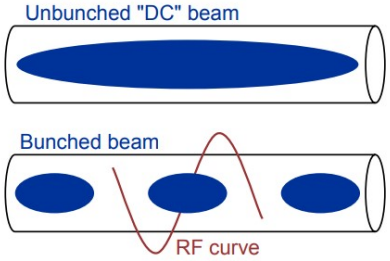

Figure 58: Beam bunching due to RF phase focusing

3.2 Harmonic number optimization

As explained in the previous section, the accelerators work with an harmonic number that defines the proportionality between the RF frequency and the revolution frequency. It has been underlined how the harmonic number is somewhat arbitrary, but it needs to match between connected machines (i.e. Booster's harmonic number is 84, Main Injector's is 588, that is 7 times 84).

While the previous thermal analysis were focused on decreasing the final temperature of the bus bars by reducing the resistance, another way to look at the problem discussed in this report would be finding a way to **reduce the current**, or, in other words, reducing the injection-extraction RF frequencies (see table 1) to feed the machine with lower RMS currents.

This can be done in different ways, one of which would be by changing the machine's harmonic number.

3.2.1 RF frequency variations

Recalling the fundamental equation $f_{RF} = h \cdot f_{rev}$ (eq. 16) and the parameters in table 1, it is possible to calculate the revolution frequency f_{rev} of the Booster in different working conditions.

Revolution frequency (or revolution period $T_{rev} = 1/f_{rev}$) is a **fixed parameter** in this problem because it depends only on the circumference of the Booster C, the speed of light c and the total energy (which is fixed as well, both for injection and extraction):

$$f_{rev} = \frac{\beta c}{C} \tag{17}$$

Where β is defined as follows:

$$\beta = \sqrt{1 - 1/\gamma^2} \tag{18}$$

$$\gamma = \frac{E_{tot}}{m_{proton}}$$

This means that it is possible to calculate the injection and extraction revolution periods for every working condition, and using them as fixed parameters to check how the injection-extraction f_{RF} range varies as the harmonic number changes. As previously stated, it is preferable to work with low f_{RF} values since they correspond to lower currents.

	Original	Present	PIP-II	
f_{rev} injection	0.3853	0.4516	0.5321	[MHz]
f_{rev} extraction	0.6287	0.6287	0.6287	[MHz]
T_{rev} injection	2.791	2.216	1.879	[μs]
T_{rev} extraction	1.591	1.591	1.591	[μs]

Table 16: Injection and extraction revolution periods

Now it is possible to use eq. 16 to calculate f_{RF} at different harmonic numbers. The only constraint to keep in mind is that the frequency has the following lower and upper bounds: $30MHz \leq f_{RF} \leq 52.8MHz$.

It is possible to calculate the $f_{RF}(t)$ curve for different operating conditions, starting from the **momentum curve** $p(t)$.

It is possible to calculate the momentum from the total energy equation:

$$E_{tot}^2 = m_p^2 \cdot c^4 + p^2 \cdot c^2 \tag{19}$$

Where $E_{tot} = KE + m_p \cdot c^2$ and $c = 1$.

Reversing the equation, it is possible to calculate injection and extraction momentum:

$$p_i = \sqrt{(\frac{KE_{inj} + m_p c^2}{c})^2 - m_p^2 \cdot c^4}$$

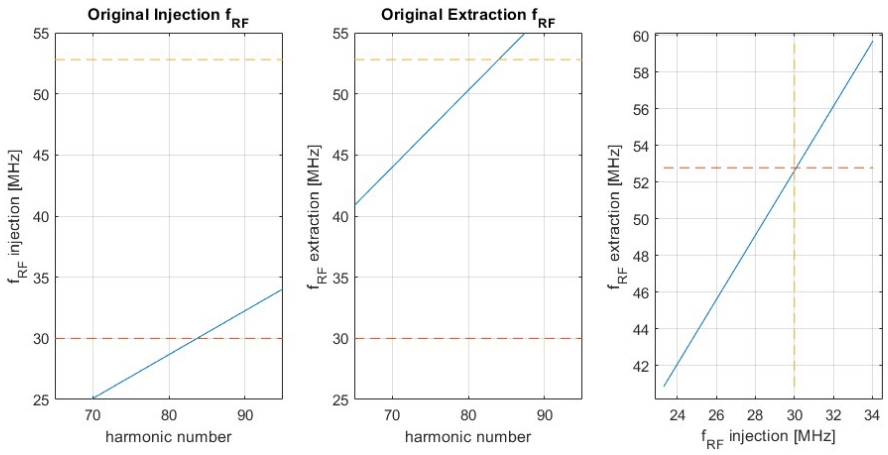

Figure 59: Original

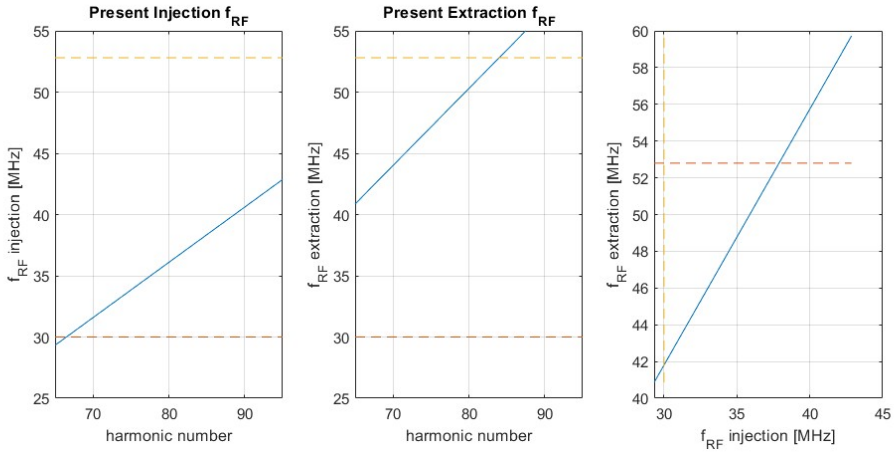

Figure 60: Present

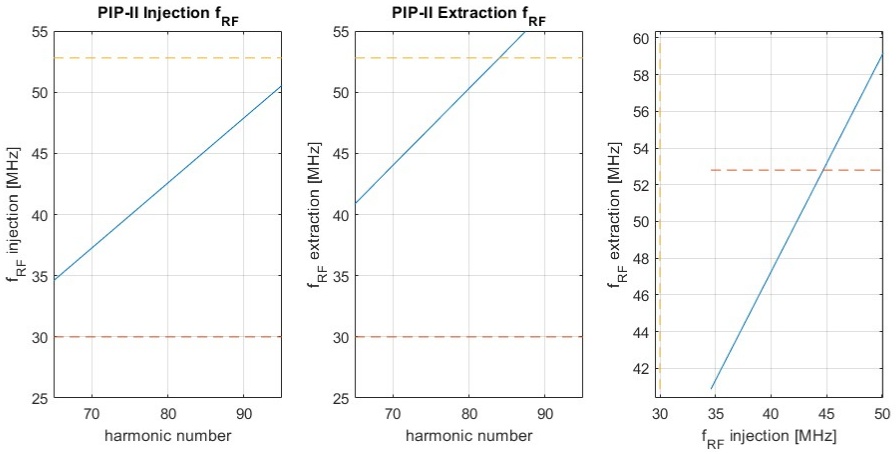

Figure 61: PIP-II

$$p_f = \sqrt{(\frac{KE_{ext} + m_p c^2}{c})^2 - m_p^2 \cdot c^4}$$

Taking into consideration the different machine frequencies f of the different eras (15Hz for original and present, 20z for PIP-II), it is possible to plot the momentum time curves assuming a sinusoidal momentum ramp:

	200MeV	400MeV	800MeV	
p_i	$6.444 \cdot 10^8$	$9.543 \cdot 10^8$	$1.463 \cdot 10^9$	[eV/c]
p_f	$8.889 \cdot 10^9$	$8.889 \cdot 10^9$	$8.889 \cdot 10^9$	[eV/c]

Table 17: Injection and extraction momentum

$$p(t) = \frac{p_f + p_i}{2} - \frac{p_f - p_i}{2} \cdot \cos \omega t \tag{20}$$

Where $\omega = 2 \cdot \pi \cdot f$.

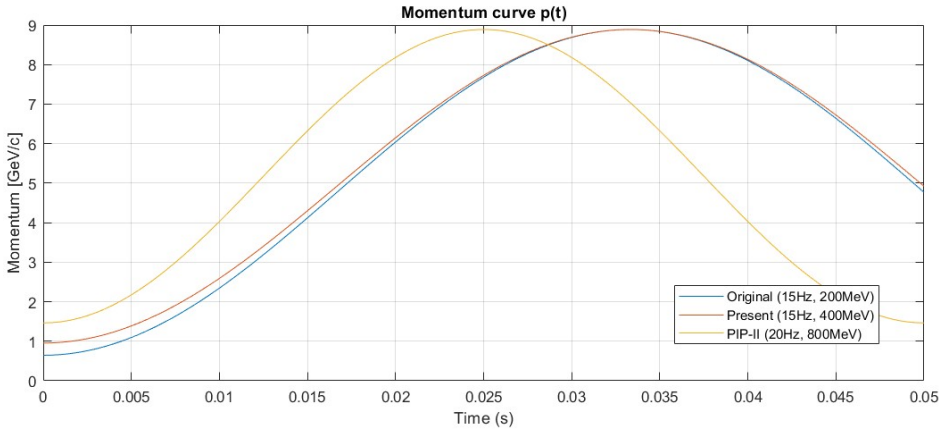

Figure 62: p(t) curves for different working conditions

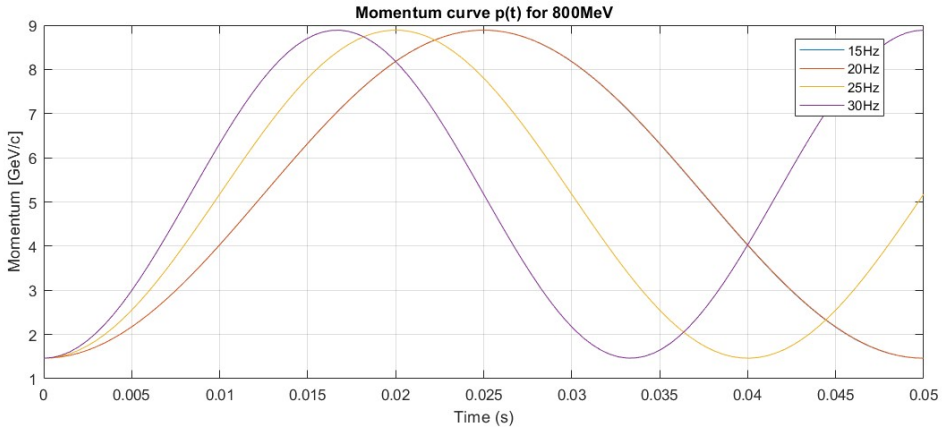

Figure 63: p(t) curves for PIP-II, changing the machine frequency

Now that the momentum curve is known, also the kinetic energy variation with time is known and hence the total energy. It is possible to calculate $f_{RF}(t)$ as follows:

$$E_{tot}^2(t) = m_p^2 c^4 + p^2(t) c^2$$

$$\gamma(t) = \frac{E_{tot}(t)}{m_p}$$

$$\beta(t) = \sqrt{1 - 1/\gamma(t)}$$

$$f_{RF}(t) = h \cdot f_{rev}(t) = h \cdot \frac{\beta(t) c}{C}$$

For the original harmonic number of $h = 84$ it is possible to plot the $f_{RF}(t)$ curves:

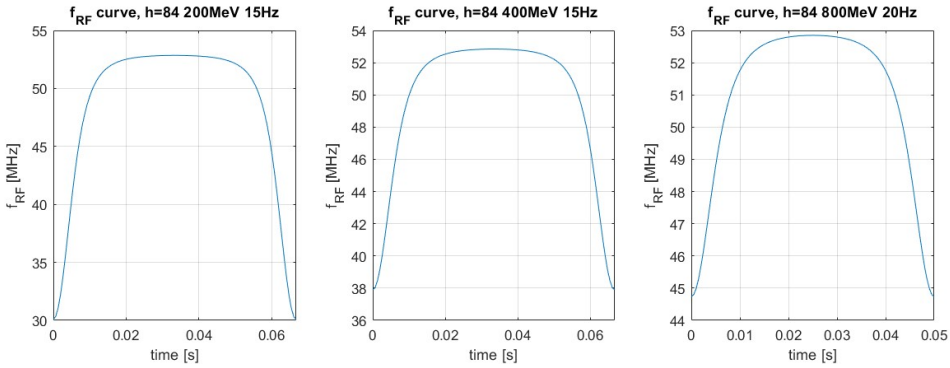

Figure 64: p(t) RF frequency curves for different working conditions

The ultimate objective of this analysis would be getting an analytical expression of the bias current as a function of the RF frequency. In order to do so, it is necessary to have some experimental data to work with.

Figure 65 shows measurements of RF frequencies and bias currents. The right figure shows the bias current as a function of RF frequency, and it is possible to obtain this expression with an interpolation.

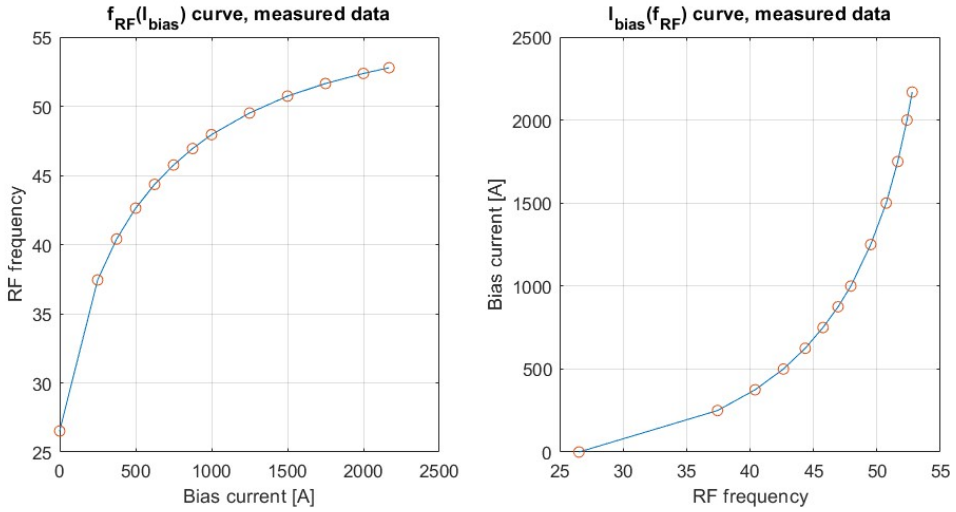

Figure 65: Experimental data

Using MATLAB's functions for fitting polynomials curve to a set of data allows to calculate a cubic interpolation (as seen in figure 66):

$$I_{bias}(f_{RF}) = 0.3155 f_{RF}^3 - 33.44 f_{RF}^2 + 1190 f_{RF} - 13920$$

And also a spline interpolation (as seen in figure 67). The most accurate result would be a spline interpolation of 12 different cubic polynomials:

$$I_{bias}(f_{RF}) = \begin{cases} 0.0657f_{RF}^3 - 0.237f_{RF}^2 + 17.65f_{RF} & \text{if } f_{RF} \in [26.52, 37.44] \\ 0.0657f_{RF}^3 + 1.916f_{RF}^2 + 35.78f_{RF} + 250 & \text{if } f_{RF} \in [37.44, 40.40] \\ 0.2865f_{RF}^3 + 2.5001f_{RF}^2 + 49.05f_{RF} + 375 & \text{if } f_{RF} \in [40.40, 42.63] \\ 0.2027f_{RF}^3 + 4.417f_{RF}^2 + 64.48f_{RF} + 500 & \text{if } f_{RF} \in [42.63, 44.35] \\ 0.0857f_{RF}^3 = 5.463f_{RF}^2 + 81.47f_{RF} + 625 & \text{if } f_{RF} \in [44.35, 45.75] \\ 0.5960f_{RF}^3 + 5.823f_{RF}^2 + 97.27f_{RF} + 750 & \text{if } f_{RF} \in [45.75, 46.94] \\ 2.567f_{RF}^3 + 7.9503f_{RF}^2 + 113.7f_{RF} + 875 & \text{if } f_{RF} \in [46.94, 47.94] \\ -0.8794f_{RF}^3 + 15.70f_{RF}^2 + 137.4f_{RF} + 1000 & \text{if } f_{RF} \in [47.94, 49.51] \\ 7.194f_{RF}^3 + 11.57f_{RF}^2 + 180.1f_{RF} + 1250 & \text{if } f_{RF} \in [49.51, 50.73] \\ -0.2585f_{RF}^3 + 37.90f_{RF}^2 + 240.4f_{RF} + 1500 & \text{if } f_{RF} \in [50.73, 51.64] \\ 12.25f_{RF}^3 + 37.20f_{RF}^2 + 308.8f_{RF} + 1750 & \text{if } f_{RF} \in [51.74, 52.78] \\ 12.25f_{RF}^3 + 64.02f_{RF}^2 + 382.7f_{RF} - 2000 & \text{if } f_{RF} \in [52.37, 52.78] \end{cases}$$

Spline interpolation equation

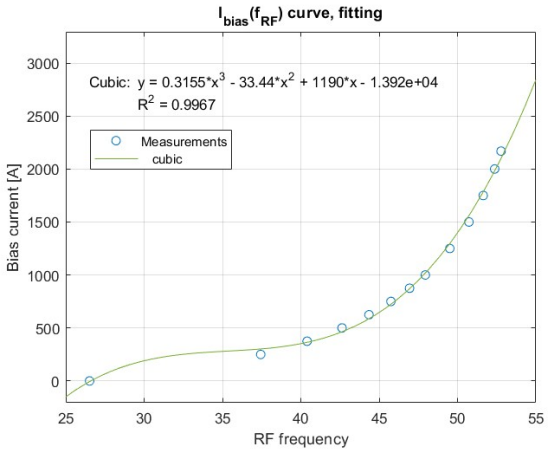

Figure 66: Cubic interpolation

The data fitting allows to obtain the **transfer function** from the f_{RF} curve to the I_{bias} curve. With this equation, it is possible to evaluate the current range for different RF frequency ranges, obtained buy changing the harmonic number- this information allows to calculate a new **RMS current**, hopefully lower than the present one (it is going to be lower, for sure, if the harmonic number is decreased).

Let us assume the harmonic number of the booster is changed to $h = 75$, while the revolution times are fixed. Following the same procedure described in this section, it is possible to obtain the new RF frequency curve (figure 68).

Figure 69 shows the different ranges of bias current for the two harmonic numbers.

Lastly, it is possible to calculate the RMS current of the two working conditions. For h=84, MATLAB's built-in rms() function allows to calculate $I_{RMS} = 1789A$, while for h=75 the result is $I_{RMS} = 770.7A$. The decrease in RMS current is definitely significant.

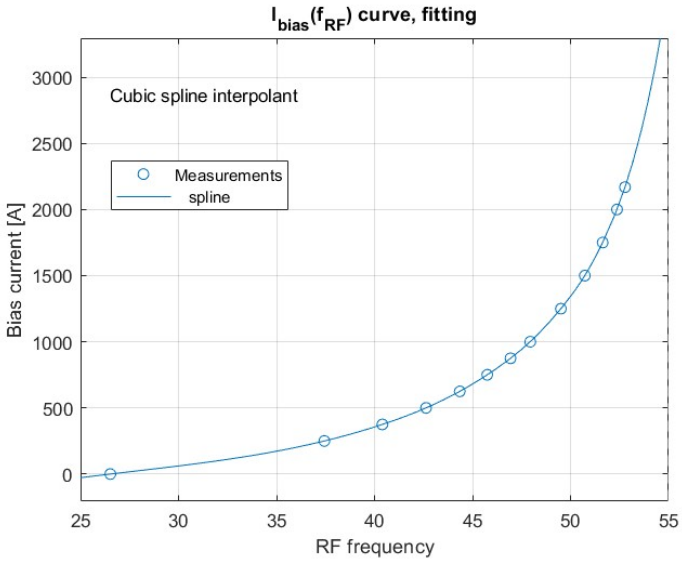

Figure 67: p(t) RF frequency curves for different working conditions

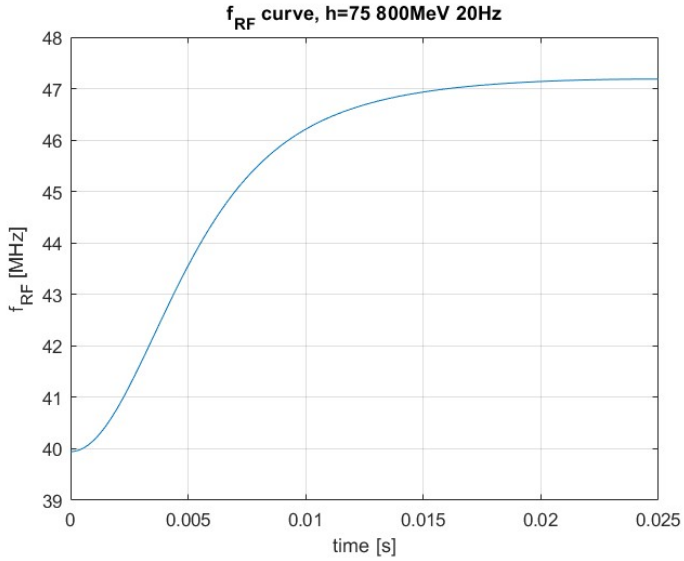

Figure 68: RF frequency range for PIP-II at h=75

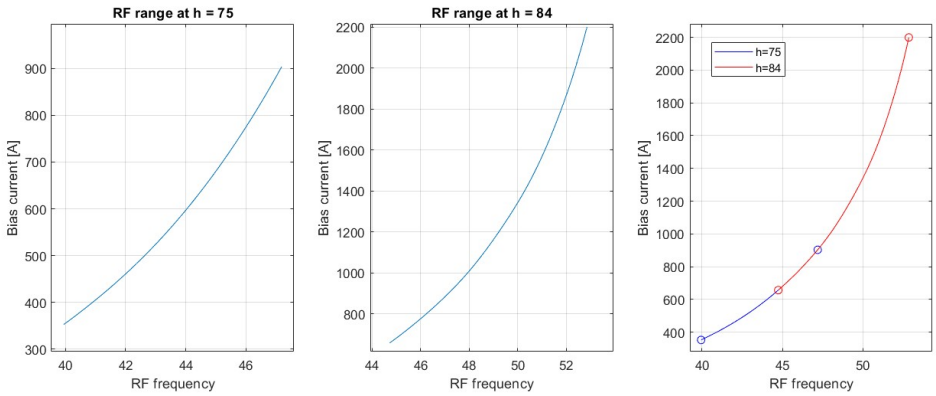

Figure 69: Comparison of different harmonic numbers for PIP-II

References

[1] Fermilab Accelerator Division. “Concepts book”. In: (2013).

[2] Matther Domeier. “Booster Bus Bar Replacement”. In: (2022).

[3] Victor Grzelak. “THE FERMILAB BOOSTER RF MODIFICATIONS FOR THE 800MEV INJECTION ERA”. In: (2023).

[4] John H. Lienhard IV and John H. Lienhard V. “A heat transfer textbook”. In: (2019).

[5] Taylor Electronics Services. “Ampacity table for copper busbars”. In: ().

[6] The Engineering Toolbox. “https://www.engineeringtoolbox.com/”. In: (2023).